

# Combined acoustic methods in monitoring the crack development in granite

Cite as: J. Appl. Phys. 135, 145104 (2024); doi: 10.1063/5.0200260

Submitted: 25 January 2024 · Accepted: 21 March 2024 ·

Published Online: 12 April 2024



View Online



Export Citation



CrossMark

Guokai Zhang,<sup>1</sup> Haibo Li,<sup>2</sup> Mingyang Wang,<sup>3</sup> Zhen Wang,<sup>3</sup> Shuxin Deng,<sup>1</sup> Fei Gao,<sup>3</sup> and Chunjiang Zou<sup>4,a)</sup>

## AFFILIATIONS

<sup>1</sup>School of Safety Science and Engineering, Nanjing University of Science and Technology, Nanjing, 210094, China

<sup>2</sup>State Key Laboratory of Geomechanics and Geotechnical Engineering, Institute of Rock and Soil Mechanics, Chinese Academy of Sciences, Wuhan, 221116, China

<sup>3</sup>School of Mechanical Engineering, Nanjing University of Science and Technology, Nanjing, 210094, China

<sup>4</sup>Department of Civil and Environmental Engineering, Brunel University London, London, United Kingdom

<sup>a)</sup>Author to whom correspondence should be addressed: [chunjiang.zou@brunel.ac.uk](mailto:chunjiang.zou@brunel.ac.uk)

## ABSTRACT

Detecting cracks of various sizes is crucial for monitoring and predicting rock failure. This study combines two acoustic methods—the passive acoustic emission (AE) and the active ultrasonic P-wave velocity to investigate the cracking process from initiation to propagation and coalescence of rocks containing pre-existing flaws, which simulate the intrinsic defects in natural rocks or rock masses, across different scales in three-dimensional space. The resultant AE activity is found sensitive to microcracks even in the early loading stage and can be divided into three stages: quiet, stable, and high growth periods. The positions of the microcracks can be obtained with the assistance of several AE sensors. It is also found that the P-wave velocity attenuation is more sensitive to macrocracks but less sensitive to microcracks. The results indicate that combining the AE and active ultrasonic-wave methods can provide comprehensive information to evaluate the damage levels and localize the internal cracks with multiple scales in the entire cracking process of rocks. The study also indicates the potential for predicting crack coalescence and failure based on the combination of these two nondestructive methods. In addition, the findings can also be applicable in the monitoring and prediction of failure in other brittle materials.

© 2024 Author(s). All article content, except where otherwise noted, is licensed under a Creative Commons Attribution (CC BY) license (<https://creativecommons.org/licenses/by/4.0/>). <https://doi.org/10.1063/5.0200260>

## I. INTRODUCTION

Natural rocks and rock masses are usually not perfectly intact but universally with some pre-existing defects and discontinuities, such as flaws, holes, joints, and even faults.<sup>1–3</sup> These pre-existing defects and discontinuities reduce the failure strength of rocks or rock masses and affect the cracking process and failure mode. The investigations on the evolution of cracks, especially the coalescence between adjacent cracks,<sup>4</sup> are essential to understanding the fracture mechanism and failure process of practical rock masses. The present study aims to provide some evidence to predict coalescence by two monitoring methods: acoustic emission (AE) and active P-wave velocity.

The crack coalescence of rocks has been comprehensively studied based on various experimental and numerical methods in the past three decades.<sup>4–14</sup> Compression tests on natural rocks and artificial rock-like specimens with machine-cut flaws are the main

methods.<sup>3,15–18</sup> Considering that mechanical properties can affect the fracturing behavior,<sup>12,19–21</sup> most previous experimental studies were conducted directly on natural rocks, e.g., marbles,<sup>7</sup> sandstones,<sup>22</sup> and granites.<sup>9</sup> Numerical simulations are usually conducted with experimental studies to verify the universality of the cracking behavior or material modes.<sup>7,23–25</sup> Two or more flaws were designed to simulate the coalescence among them physically, and the pre-existing flaws with identical or different inclination angles might be coplanar or non-coplanar,<sup>9,22</sup> the results of which showed that the flaw inclination angle and the bridge angle significantly affected the strength and coalescence mode under uniaxial compression.

Photographic techniques are the main tools to observe and monitor the cracks, while the initiation and development of internal cracks behind the surface are not adequately studied. CT scanning techniques were then utilized to observe the internal cracks.<sup>26</sup> However, due to the high propagation speed of cracks, the scanning

20 April 2024 06:41:29

speed is not fast enough to capture the real-time cracking process of brittle materials. In addition, the precision of normal CT scanners is not capable of detecting some microcracks with scales smaller than micrometers. Therefore, the acoustic emission (AE) technique was applied in this field. It can provide a relatively higher sample rate and resolution to detect the position and count of these microcracks in the early stage of rock failure in real-time.<sup>27–35</sup> The quick localization of hypocenters or microcracks inside the rock samples is superior to other methods. Even in biaxial and triaxial tests,<sup>36–38</sup> which involve liquid oil to produce confining pressure, localization can also be conducted since the P-wave can propagate in liquids. Many experimental studies were conducted to investigate the spatial distribution of AE hypocenters during the failure process of intact rocks,<sup>2,30,34,39–42</sup> after the pioneering work done by Lockner in 1993.<sup>43</sup> The results showed that the crack evolution identified from the localization of AE hypocenters coincided well with the actual failure pattern, which might inspire the prediction of the failure of underground rock masses.<sup>44</sup> Diederichs *et al.* (2004)<sup>28</sup> found that the onset of damage coincided with AE counts first rising above the background, and crack coalescence corresponds to the deviation of log-linear accumulation of AEs. Vilhelm *et al.* (2008)<sup>30</sup> observed that the interaction and nucleation of fractures could be indicated by AE events. However, rock masses generally contain pre-existing discontinuities or defects, and the failure process is significantly different from that of intact rocks. Lei *et al.* (2004)<sup>45</sup> studied the effect of natural faults on the rock fracture process. It was indicated that the precursory anomalies associated with rock failure strongly depended on fault heterogeneity and geometries.<sup>46</sup> Li *et al.* (2019)<sup>47</sup> investigated the crack coalescence process of rocks with two pre-cut flaws under hydraulic fracturing pressure, and the hypocenter locations coincided well with visually observed white patching. Compared with the tensile failure in hydraulic fracturing, the coalescence of pre-existing flaws under compressive loading is more common, which is the main part of the present research.

Active elastic wave testing is another method used to assess the average damage induced by the crack increment and growth based on the wave attenuation in the frequency and amplitude.<sup>48</sup> It is more practical in engineering applications in rock masses and geological bodies due to the quantitative measurement of the overall damage.<sup>48–51</sup> The correlations between the failure process and the wave velocity were studied on different materials, including borosilicate glass and Seljadur basalt,<sup>40</sup> granite,<sup>35,46</sup> low-porous carbonate rock,<sup>52</sup> granulite samples,<sup>53</sup> low-porosity sandstone,<sup>32</sup> and mortar.<sup>54</sup> Changes in  $V_p$  (P-wave velocity) and  $V_s$  (S-wave velocity) are strongly correlated with the applied loading in the principal stress directions. The increase in the velocity can be found in the initial loading stage due to the closure of microcracks, while the decrease happens around the peak loading.<sup>33,55</sup> By multiple parallel sensors, the changes in the velocity field can be drawn based on the

periodic P-wave surveys among multiple ray paths.<sup>41</sup> Wave attenuation was also investigated on the failure process of non-intact rocks containing flaws that simulated the failure of natural rocks.<sup>56</sup> Modiriasari *et al.* (2017)<sup>57</sup> reported that the crack initiation of a flawed limestone was correlated to the sharp reduction in the transmitted wave amplitude, and the distinct minimum of the transmitted wave amplitude occurred close to crack coalescence by the active ultrasonic monitoring technique.

However, the acoustic identification of the crack coalescence process and the different sensitivities between the AE and P-wave velocity methods are not comprehensively studied, especially the interaction between the wave velocity and the internal crack growth. Therefore, in this paper, passive acoustic emission and active ultrasonic testing are jointly applied to monitor cracks and wave velocity of granite rocks containing a single and two parallel flaws. The loading processes and cracking behavior, including the coalescence, are characterized by AE parameters and P-wave velocities. In particular, the time-spatial evolution of AE hypocenters is localized to trace the internal crack propagation, providing us with a novel way to understand the failure process. Although the experimental material in the present study is granite, the conclusions can also be applied to other materials with a similar brittleness,<sup>58</sup> such as sandstones,<sup>32</sup> gypsum, concrete, and ceramics.

## II. METHODS

### A. Rock material and sample preparation

Fine-grained granite with low porosity is used to prepare the experimental samples. The physical and mechanical properties of the granite samples obtained by standard testing methods suggested by International Society for Rock Mechanics (ISRM) are shown in Table I. It is a hard rock with an average density of about 2789 kg/m<sup>3</sup> and P-wave velocities ranging from 4020 to 4232 m/s. The granite comprises 35.9% microcline, 30.1% quartz, 26.1% calcian albite, 5.3% biotite, and 2.6% others given by the x-ray diffraction (XRD) analysis. The optical microscopic observation shows very few strip-shaped microcracks distributed in the granite (Fig. 1). The scanning electron microscope (SEM) image demonstrates the well interlocking among mineral grains.

In the present study, prismatic samples containing two open parallel flaws with the dimensions of 60 × 120 × 40 mm<sup>3</sup> (width × length × thickness) are fabricated by a high-pressure water-jet machine. Herein, “flaw” means the artificial open crack cut in the intact samples before testing. The opening of the flaw is about 1 mm, with a length ( $2a$ ) of 15 mm. A smooth and precise boundary of the flaw can be obtained by the water-jet cutter.<sup>59,60</sup> For the double-flawed specimen, the flaw angle  $\alpha$  is the angle between the normal direction of the flaw and the axial direction, and the bridging angle  $\beta$  is the counterclockwise angle between the axial line and the horizontal reference line. The length ( $2b$ ) of the

**TABLE I.** Physical and mechanical properties of granite samples.

Rock	Density (kg/m <sup>3</sup> )	Uniaxial compression strength (MPa)	Elastic modulus (GPa)	Poisson's ratio	P-wave velocity (m/s)
Granite	2789	272–284	61.8–64.2	0.20–0.23	4020–4232

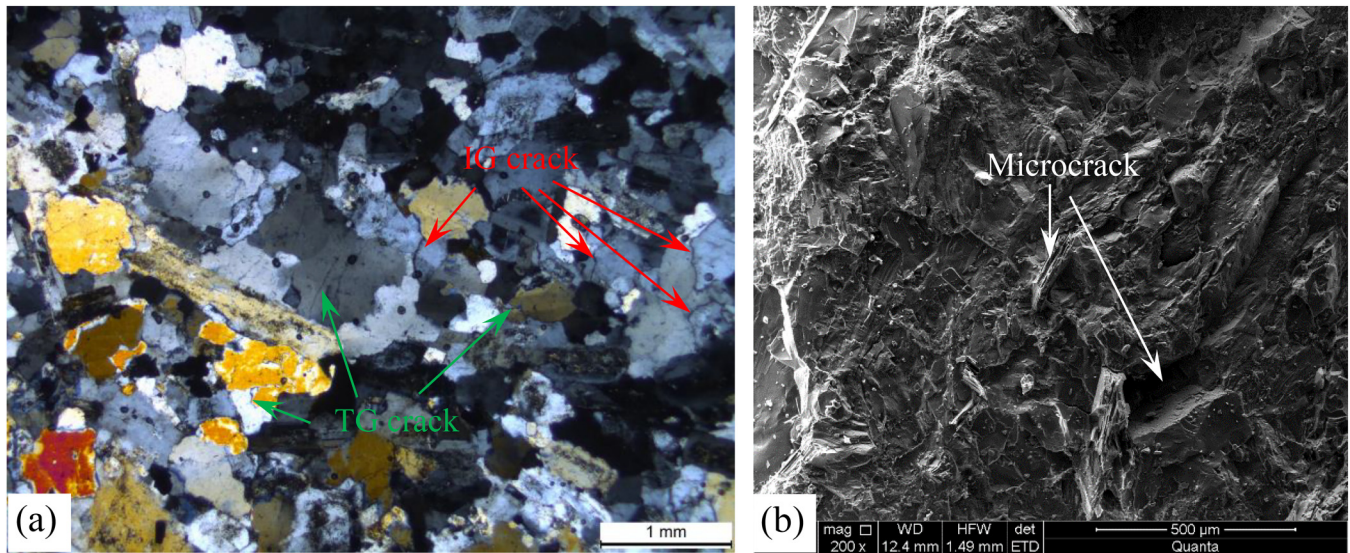


**FIG. 1.** (a) Optical microscopic observation of the granite sample (TG—transgranular, IG—intergranular); (b) SEM image showing the microstructure of the granite sample.

ligament line between the flaws is 18 mm. The samples with a single flaw or two parallel flaws are marked by  $S\alpha$  and  $D\alpha-\beta$ , respectively, as shown in Fig. 2 and Table II.

### B. Testing system

The rock samples are subjected to uniaxial compression loading using an MTS815 testing system with a maximum loading capacity of 4600 kN. The displacement control mode implements the uniaxial compression tests with a constant rate of 0.001 mm/s,

while the axial displacement during the loading process is measured using an axial extensometer. As shown in Fig. 3, active ultrasonic transmission testing and passive acoustic emission (AE) are synchronously used to measure the P-wave attenuation and acoustic emission and, hence, monitor the internal crack development. P-wave velocities along different directions are measured simultaneously with the AE signals during the test. Multiple AE characteristic parameters (cracking event, cumulative energy, waveform frequency, hit count) are analyzed to monitor the micro-cracking behavior by eleven wideband (125–750 kHz) Nano30 transducers

20 April 2024 06:41:29

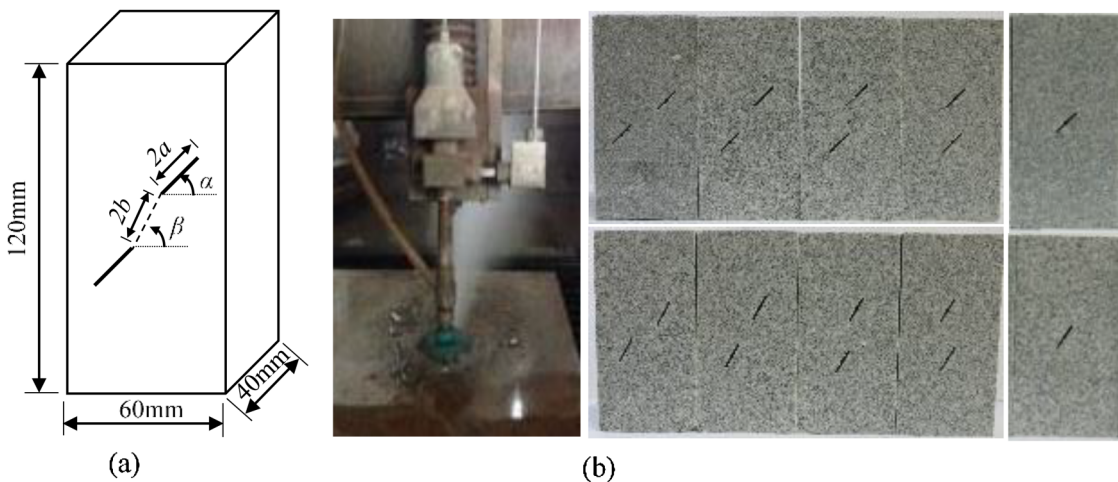
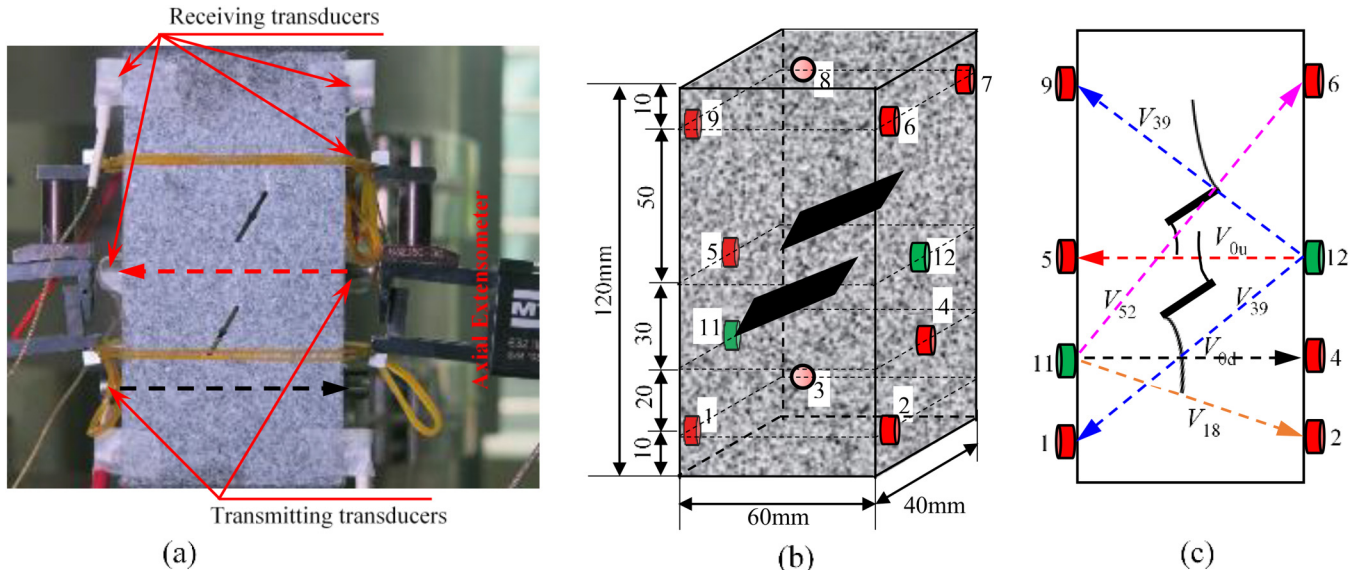


**FIG. 2.** (a) The geometry of rock samples containing two parallel flaws; (b) the high-pressure water-jet system and the prepared granite samples.

TABLE II. Flaw geometries of granite samples.

Sample	Mark	Flaw angle $\alpha$ (°)	Bridging angle $\beta$ (°)	2a (mm)	2b (mm)
Double flawed	D $\alpha$ - $\beta$	45, 60	30, 60, 90, 120	15	18
Single-flawed	S $\alpha$	45, 60	N/A	15	N/A



20 April 2024 06:41:29

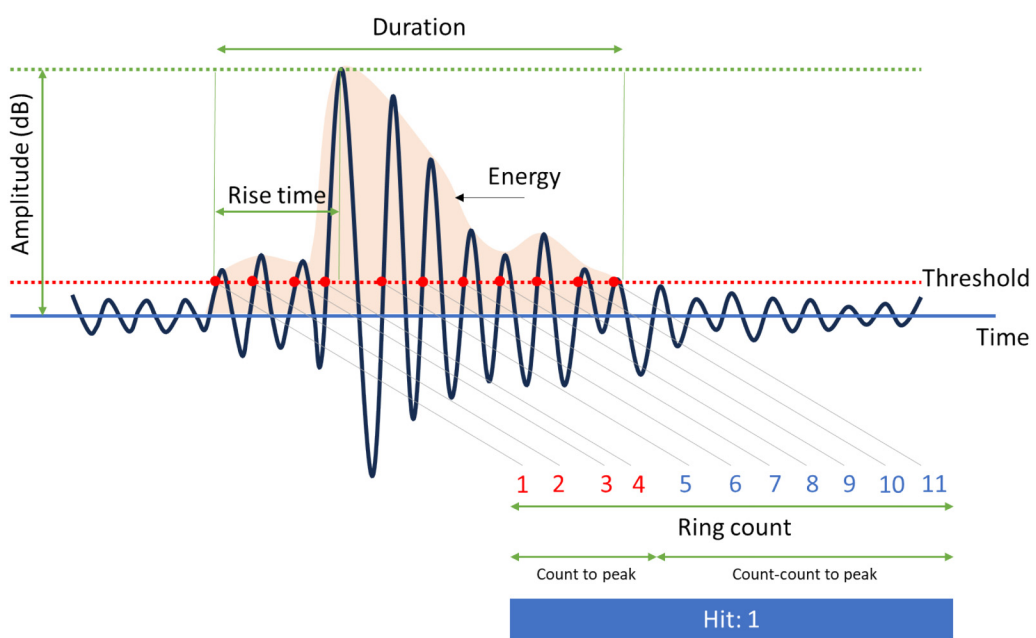


FIG. 4. Main parameters in acoustic emission testing.

FIG. 3. (a) Experimental setup; (b) eleven piezoelectric transducers attached on three sides of the rock sample (green—active ultrasonic transducer, red—passive acoustic sensor); (c) the diagram of P-wave propagation paths.

attached on three sides of a sample using silicone grease as a coupling agent. The diameter of the transducers is 8 mm. During the loading process, AE signals are monitored continuously at a sampling rate of 10 MHz to improve the resolution of the first arrival time.

Meanwhile, the P-wave velocity is simultaneously measured at a certain interval. The previous AE transducers (No. 1 to No. 9) also act as the receivers in this test. The testing interval of P-wave velocity is adjustable with 20 s at the initial loading stage and less than 5 s at the violent cracking stage. As shown in Fig. 3(b), nine transducers (sensors No. 1 to No. 9, red) are used to receive the AE signals with a preamplifier at a gain of 40 dB. A wide bandpass filter with a 10 kHz–3 MHz bandwidth is set to record the full waveform. Two ultrasonic-wave transducers (sensors No. 11 and No. 12, green) acting as the transmitter are used to measure the periodic P-wave velocities between the transmitter and the receiver—the AE transducer (No. 1 to No. 9). The transmitter is excited by a built-in high-voltage pulser to stimulate elastic wave pulses. P-wave velocity is calculated through the time lapse between the transmitting and receiving waveform signals. The schematic diagram of P-wave propagation paths is displayed in Fig. 3(c), including lateral velocity ( $V_{0u}$ ,  $V_{0d}$ ) in different cross sections. P-wave velocities along the ray paths at 18°, 39°, and 52° inclination angles to the horizon are marked by  $V_{18}$ ,  $V_{39}$ , and  $V_{52}$ , respectively. Sensor pairs No. 5 and No. 12 are used to monitor the initiation and coalescence of cracks in the bridging area, while sensor pairs No. 4 and No. 11 are used to monitor the downward propagation of cracks initiated from the flaw-tip. Since the position of each transducer is fixed, the relative distances between the ultrasonic-wave transducer and the receiver are then determined. The wave velocities of different paths can be differentiated and calculated by comparing the time length of receiver signals.

The typical AE parameters, including duration, waveform energy, hit count, and ring count, are shown in Fig. 4. The duration is the time difference between the start and end rings. The waveform energy is the integration of the envelope covering the waveform regarding the duration. In the present study, the amplitude is the

waveform recorded by the oscilloscope after the amplifier. The ring count is the number of rings with an amplitude higher than the threshold for a single AE event or hit. The sample rate is the key to obtaining enough information from the analog AE signal in the digital data acquisition system. Since the frequencies interested in rock cracking processes usually range from 100 to 500 kHz, the sample rate of 10 MHz used in this research can provide a wide bandwidth in the frequency domain. Meanwhile, the waveform length is  $1024\ \mu\text{s}$ , indicating a minimum capacity of 1024 AE events in 1 s. Therefore, the average peak frequency (APF) is defined as the ratio of the peak frequency summation to the event number every second to evaluate the variation trend of the peak frequency.

### III. RESULTS

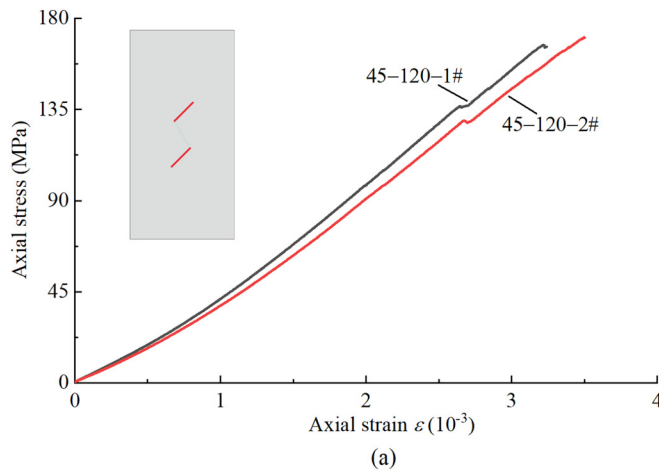
This section comprises two components: the mechanical and acoustic behavior during the crack processing of the samples. First, stress-strain curves of typical samples and their corresponding mechanical properties are examined in detail, including peak stress, peak strain, deformation modulus, elastic modulus E, crack initiation stress, and the ratio of crack initiation stress to peak stress. Second, the signal obtained from monitoring the cracking process is analyzed synthetically using active and passive acoustic methods.

#### A. Mechanical behavior

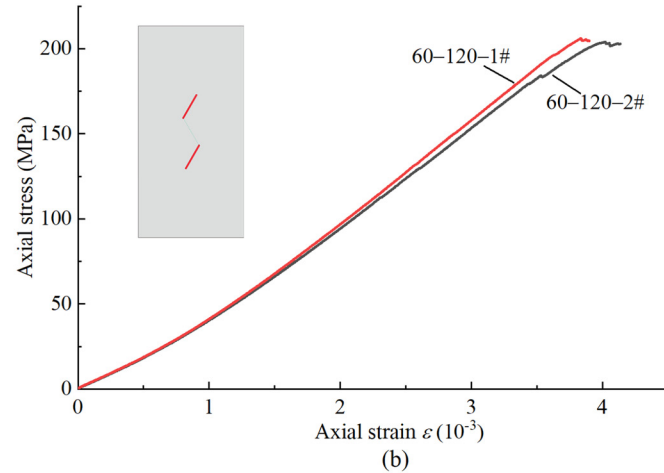
##### 1. Stress-strain curves of flawed samples

Two types of double-flawed granite samples, denoted by D45–120 and D60–120 ( $\alpha = 45^\circ$ ,  $\beta = 120^\circ$ , and  $\alpha = 60^\circ$ ,  $\beta = 120^\circ$ ) are tested by uniaxial compression. The homogeneity and repeatability of the granite are evaluated by using two parallel samples. The stress-strain curves are plotted in Fig. 5, which shows that the stress-strain curves for rock samples with the same flaw geometries are consistent, indicating the homogeneity and good repeatability of the granite on mechanical behavior.

20 April 2024 06:41:29



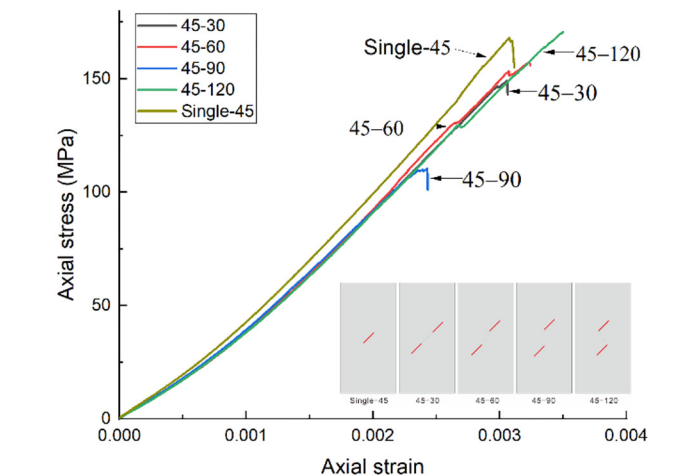
(a)



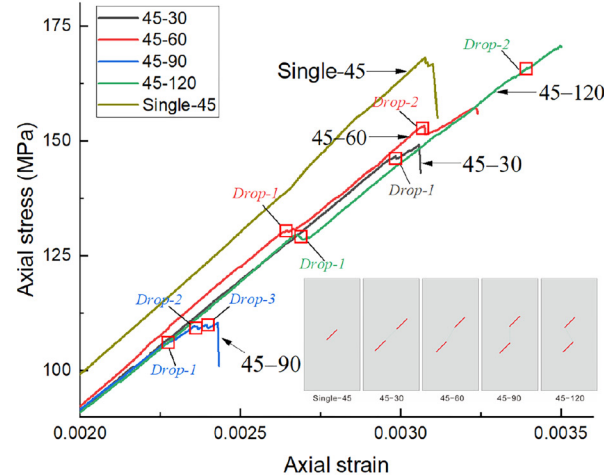
(b)

**FIG. 5.** Comparison of the stress-strain curves in each group: (a) D45–120 samples and (b) D60–120 samples.

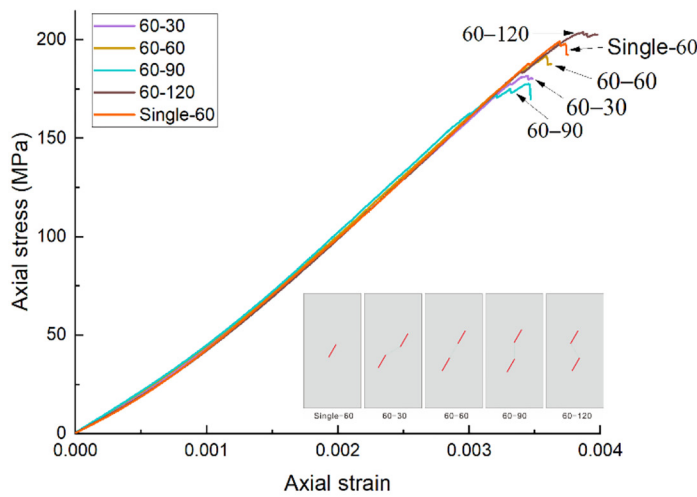
More samples containing single or double flaws are tested to evaluate the influence of the flaw geometry on the mechanical behavior. The corresponding stress-strain curves are shown in Fig. 6. It is found that flaw inclination angle, bridging angle, and flaw number all affect the mechanical behavior. However, these effects are not conspicuous in the first half. Like intact samples, all the stress-strain curves behave somewhat nonlinearly at the initial loading stage, which is believed to be caused by the pressure-induced closure of original microcracks.<sup>40</sup>



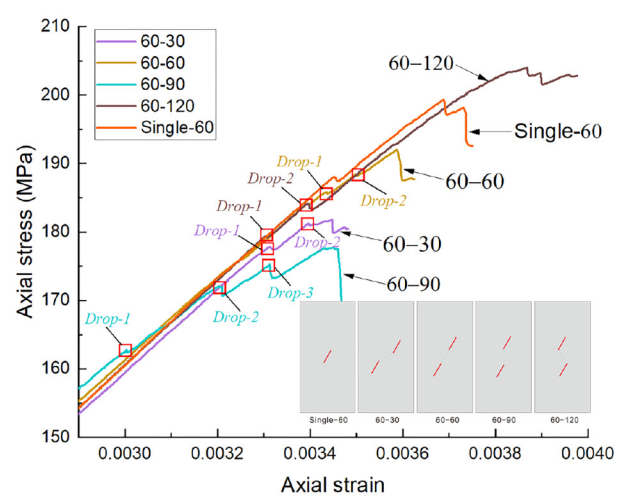
(a)



(b)



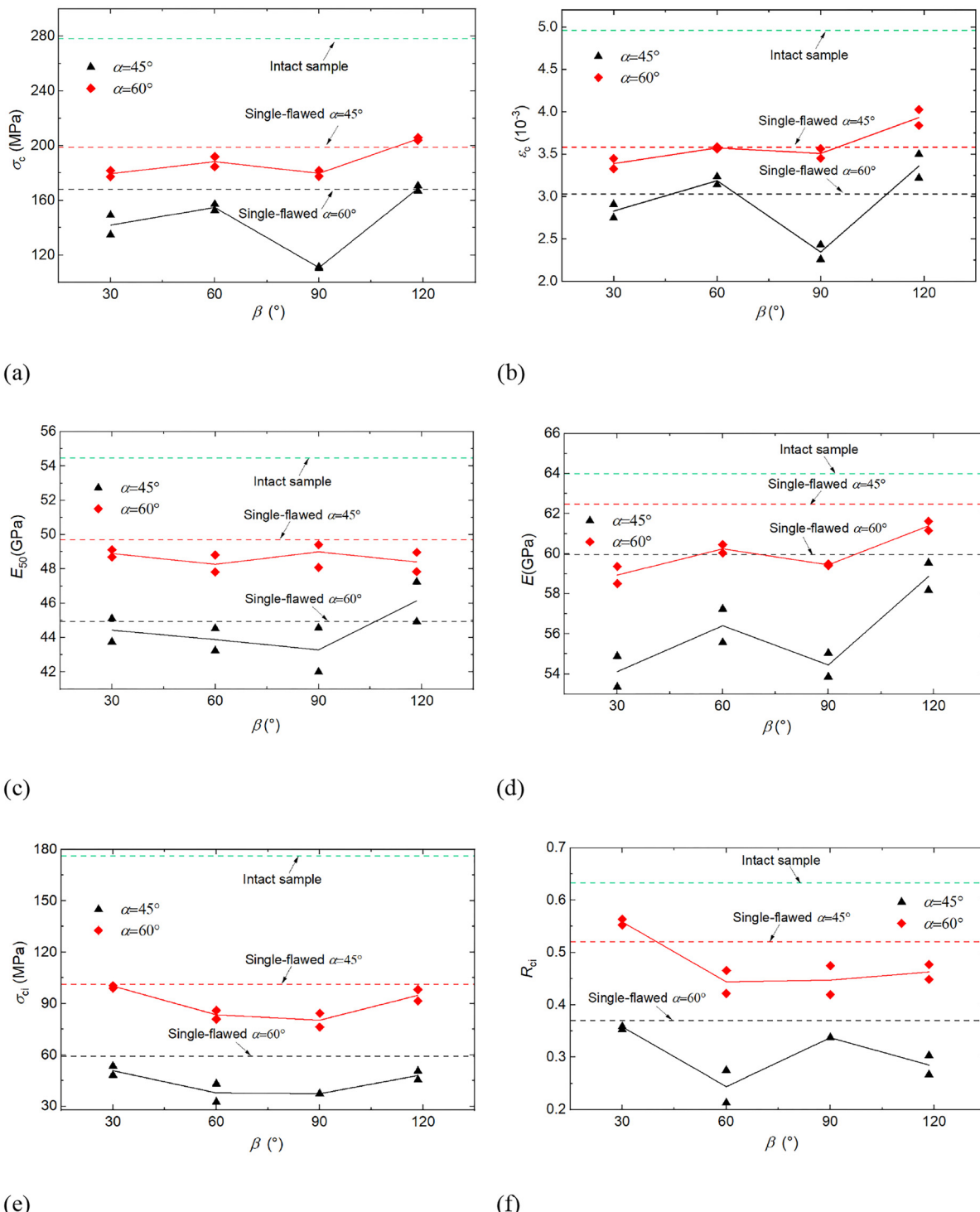
(c)



(d)

20 April 2024 06:41:29

**FIG. 6.** (a) Stress-strain curves for flawed granite samples with the flaw inclination angle  $45^\circ$  and (b) the magnitude image showing the stress drops of the stress-strain curves; (c) stress-strain curves for flawed granite samples with the flaw inclination angle  $60^\circ$  and (d) the magnitude image showing the stress drops of the stress-strain curves.



20 April 2024 06:41:29

**FIG. 7.** Effect of the flaw angle and bridging angle  $\beta$  on the mechanical properties, including (a) peak strength  $\sigma_c$ , (b) peak strain  $\varepsilon_c$ , (c) deformation modulus  $E_{50}$ , (d) elastic modulus  $E$ , (e) crack initiation stress  $\sigma_{ci}$ , and (f)  $R_{ci}$  (ratio of  $\sigma_{ci}$  to  $\sigma_c$ ). The green line represents the corresponding value of the intact sample, the red line represents the corresponding value of the sample with a  $60^\circ$  single flaw, and the black line represents the corresponding value of the sample with a  $45^\circ$  single flaw.

$\beta=120^\circ$  show a distinct plasticity deformation before the peak failure, especially for the D60–120 sample. These two characteristics might be the factors that produce higher failure stress in the D45–120 and D60–120 samples.

Multiple stress drops, marked by the square box in Fig. 6, may appear before the peak stress for the double-flawed samples. For the D60–90 sample in Fig. 6(d), the first stress drop, marked by *Drop-1*, occurs at 162.6 MPa uniaxial stress, accompanied by the reduction in stiffness reflected by the reduced slope of the following stress-strain curve, while the second and third stress drops with a shorter gap, marked by *Drop-2* and *Drop-3*, follow the first drop. The stress drop is attributed to the macroscopic manifestation of accelerated crack propagation.<sup>35</sup> After each stress drop, the sample stiffness is reduced, but the inelastic deformation increases. For other double-flawed samples, the first stress drop occurs much later than the D60–90 sample, as shown in Fig. 6(d). A similar trend is found for the double-flawed samples with the inclination angle of  $45^\circ$  in Fig. 6(b).

## 2. Other mechanical properties

Two groups of samples with the flaw inclination angles  $45^\circ$  and  $60^\circ$ , respectively, are used to test the variation in main mechanical properties with the bridging angle  $\beta$ . Such mechanical properties include peak stress  $\sigma_c$ , peak strain  $\varepsilon_c$  (the axial strain value at the peak stress), nominal deformation modulus  $E_{50}$ , nominal elastic modulus  $E$ , crack initiation stress  $\sigma_{ci}$ , and the corresponding stress ratio  $R_{ci}$  (the ratio of  $\sigma_{ci}$  to  $\sigma_c$ ). Here, the nominal deformation modulus  $E_{50}$  is defined as the ratio of the 50%  $\sigma_c$  to the corresponding strain, and  $\sigma_{ci}$  is defined as the stress corresponding to the onset of the AE event (AE counts first rising above background).

The existence of the flaws and their orientation has a significant impact on these mechanical properties, as illustrated in Fig. 7. The intact samples without flaws generally have the highest value for most mechanical properties. The minimum  $\sigma_c$  of the flawed sample (D45–90) is 110.4 MPa with a reduction of 60% compared to intact granite. The peak stress  $\sigma_c$  changes undulated with  $\beta$ , and the  $\sigma_c$  of flawed samples with  $\alpha=60^\circ$  is higher than

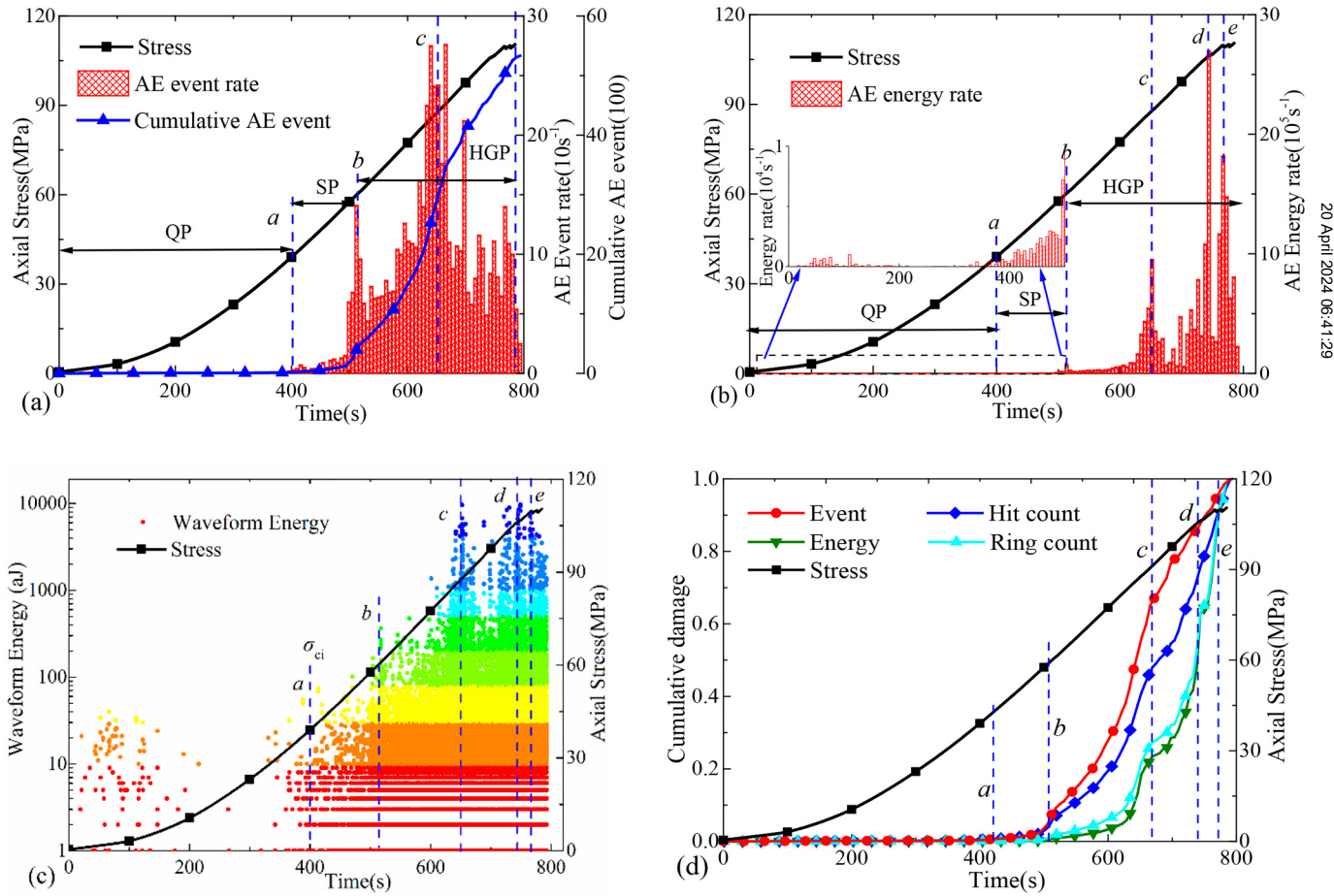


FIG. 8. The variations in AE parameters for sample D45–90: (a) event rate; (b) energy rate; (c) the characteristic of AE energy; (d) rock damage inferred by the AE event, hit count, energy, and ring count.

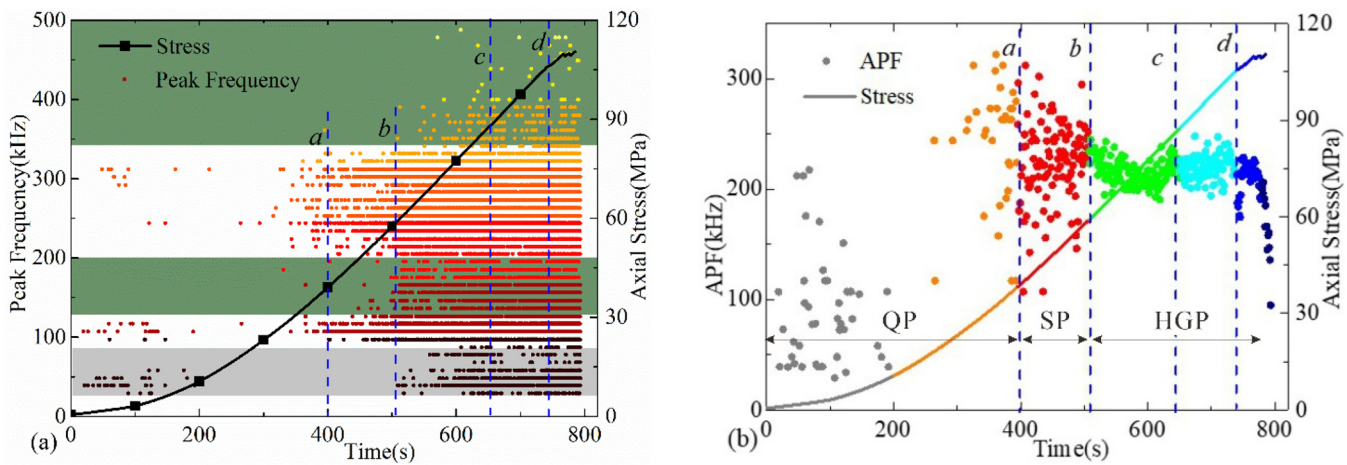


FIG. 9. (a) Peak frequency and (b) average peak frequency (APF) of AE signals in the frequency domain for sample D45-90.

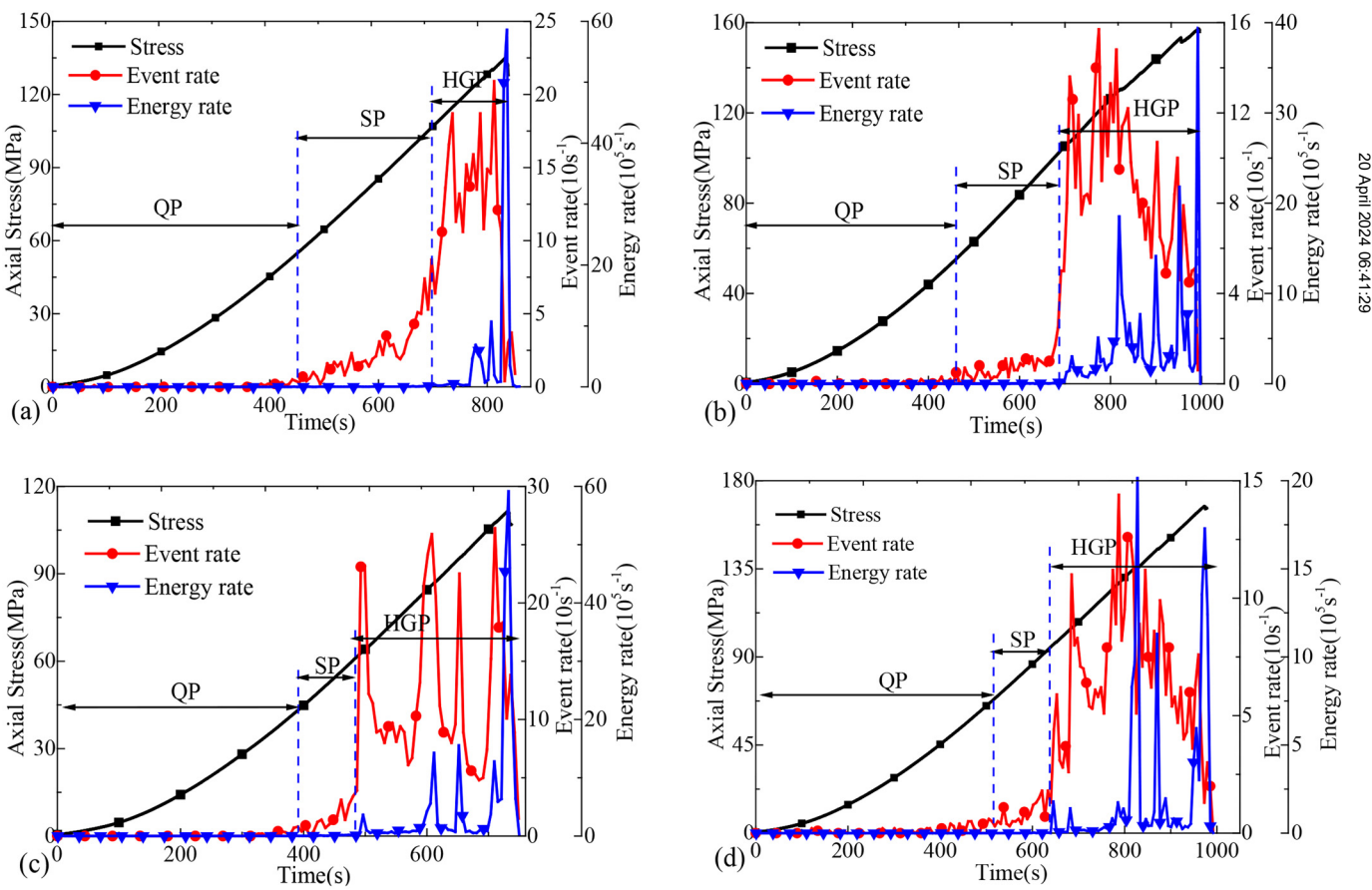


FIG. 10. The comparisons of the event and energy rate for granite samples containing two parallel flaws with  $\alpha = 45^\circ$  (a)  $\beta = 30^\circ$ ; (b)  $\beta = 60^\circ$ ; (c)  $\beta = 90^\circ$ ; (d)  $\beta = 120^\circ$ .

those with  $\alpha = 45^\circ$ . However, the latter has a slightly higher data scattering.

The peak strain  $\varepsilon_c$  is a precursor of disastrous rock failure. The variation in  $\varepsilon_c$  and the elastic modulus  $E$  of the double-flawed samples against bridging angle  $\beta$  is roughly consistent with  $\sigma_c$ . The  $\varepsilon_c$  ranges between 0.226% and 0.35% ( $\alpha = 45^\circ$ ) or 0.333% and 0.402% ( $\alpha = 60^\circ$ ). The moduli of flawed samples with  $\alpha = 60^\circ$  are normally higher than those with  $\alpha = 45^\circ$  regardless of the bridging angle. The elastic modulus  $E$  ranges from 53.35 to 61.6 GPa, and the maximum reduction reaches up to 17% compared to the intact granite. In contrast, the variation range of the deformation modulus  $E_{50}$  is narrower than the elastic modulus  $E$ .

The onset of crack initiation corresponding to the accumulation of rock damage is usually identified as the lower bound of *in situ* strength of engineering rock mass.<sup>28</sup> The crack initiation stress  $\sigma_{ci}$  of these double-flawed samples is shown in Fig. 7(e).  $\sigma_{ci}$  decreases with the bridging angle  $\beta$  until the overlapping of flaws happens, and the single-flawed samples have the highest  $\sigma_{ci}$ . The

$R_{ci}$  of the double-flawed granite ranges from 0.21 to 0.37 ( $\alpha = 45^\circ$ ) or from 0.42 to 0.56 ( $\alpha = 60^\circ$ ).

## B. Acoustic behavior

### 1. AE characteristics

This section discusses the variation in some typical AE parameters, including AE event rate, cumulative AE event AE energy rate, waveform energy, hit count, and ring count. Figure 8 illustrates the variation in these AE parameters with the axial load for double-flawed sample D45-90. According to the AE signal, the cracking process can be divided into three typical stages: QP—quiet period (no obvious AE event nearly), SP—stable period (event rate and energy rate at a low level), and HGP—high growth period (event rate at a significantly high level).

In the first half of the QP stage, only a few discrete AE signals with energy below 40 aJ emerge (Fig. 8), which is observed similar to the intact granite. Afterward, the AE event becomes relatively quiet. When the stress reaches 38 MPa ( $0.33\sigma_c$ , marked as  $a$  in

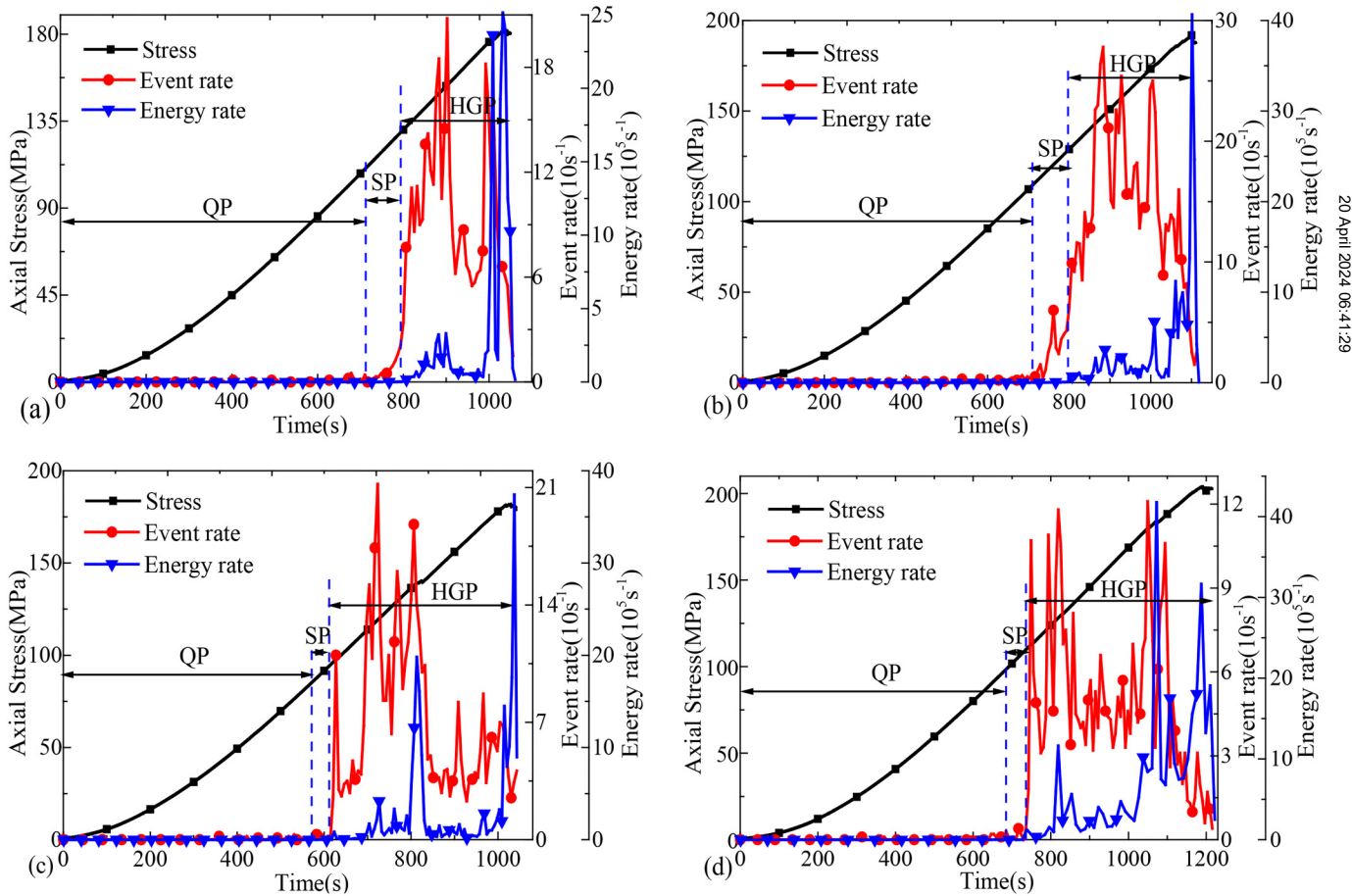


FIG. 11. The comparisons of AE event rate and energy rate for granite samples containing two parallel flaws with  $\alpha = 60^\circ$  (a)  $\beta = 30^\circ$ ; (b)  $\beta = 60^\circ$ ; (c)  $\beta = 90^\circ$ ; (d)  $\beta = 120^\circ$ .

**TABLE III.** Characteristic stress corresponding to different parameters.

Flaw angle $\alpha$ (°)	Bridging angle $\beta$ (°)	Beginning of HGP		First stress drop		Maximum event rate		Maximum energy rate		Event number	Cumulative energy (aJ)
		$\Sigma$ (MP)	$\sigma/\sigma_c$	$\Sigma$ (MP)	$\sigma/\sigma_c$	$\Sigma$ (MP)	$\sigma/\sigma_c$	$\Sigma$ (MPa)	$\sigma/\sigma_c$		
45	30	107.1	0.79	123.8	0.92	130.4	0.97	134.8	1.00	3739	15 628 065
45	60	104.6	0.67	104.6	0.67	119.8	0.76	156.3	0.99	4458	24 443 494
45	90	61.2	0.55	95.8	0.86	107.4	0.96	111.3	1.00	5220	24 010 546
45	120	95.1	0.57	97.9	0.59	128.8	0.77	135.9	0.81	3891	22 664 976
60	30	130.5	0.72	177.4	0.98	153.5	0.84	181.7	1.00	4007	16 432 129
60	60	137.1	0.71	176.1	0.92	146.9	0.76	191.5	1.00	7793	20 871 510
60	90	95.3	0.52	139.1	0.76	119.1	0.65	181.8	1.00	4821	22 383 078
60	120	96.5	0.47	129.7	0.64	179.6	0.88	183.5	0.90	3778	27 859 818
45	...	132.5	0.78	147.9	0.80	153.6	0.91	155.2	0.92	5238	28 356 920
60	...	158.6	0.80	188.0	0.94	174.1	0.87	198.1	1.00	5414	29 889 282

**Fig. 8**), the cracking event begins to increase gradually, accompanied by the dramatic rise of waveform energy [**Fig. 8(c)**], representing the initiation of micro-cracks. In this period, the waveform energy increases sharply from 70 to 300 aJ. The dramatic increase in the AE event rate at 59 MPa marks the end of the SP stage. In the HGP stage, the event rate reaches the maximum at 91 MPa (marked by *c* in **Fig. 8**), accompanied by a significant bulge of AE energy. Multiple events or energy rate bulges appear during the HGP stage before the peak stress, and the energy changes more violently. Before the peak failure, several stress drops can be found coinciding with a significant energy bulge and reduction in the tangent modulus attributed to the rapid growth of macrocracks. Based on the assumption that rock damage is correlated to the AE number, the damage evolution inferred from the event rate, hit count, energy, and ring count is shown in **Fig. 8(d)**. Rock damage accumulates at a low speed at the SP stage and a much higher speed at the HGP stage.

The result indicates that AE parameters can identify the microcrack initiation well, but the violent failure process around the failure point is hard to identify for brittle rocks. However, as the energy released by each cracking event differs significantly (ranging from below 40 to 10 000 aJ), it is inappropriate to assume that the damage contribution induced by each event is identical.

Apart from the AE parameters in the time domain, the signal characteristics in the frequency domain, which is the frequency spectrum of acoustic waveforms, are also helpful in understanding the cracking mechanism.<sup>61,36</sup> The peak frequency corresponds to the maximum value of the frequency-energy spectrum. The peak frequencies of each recorded AE event are determined and illustrated with the event time for the sample D45–90, as shown in **Fig. 9(a)**. In the figure, the points representing the peak frequencies are commonly overlapped due to many similar frequencies. To quantitatively analyze the variation trend of the peak, average peak frequency (APF), which is the ratio of the peak frequency summation to the event number in every second, is calculated, as shown in **Fig. 9(b)**. The variation in the peak frequency at different stages is stated below in detail.

In the QP stage, the peak frequency has two significantly different sections. In the first half section, most AEs have a peak frequency

below 125 kHz, probably induced by the closure of the pre-existing microcracks. In the second half section, the APF increases swiftly due to the micro-crack initiation before time *a* (**Fig. 9**). In the SP stage, the peak frequency ranges from 97 to 322 kHz, showing somewhat higher scattering but starting to converge at the end of this stage. In the HGP stage, the bandwidth of the APF becomes narrower and relatively stable in the range of 190–250 kHz. The APF keeps constant from time *c* to *d* and then decreases significantly after time *d*. The APF scattering increases again.

Generally, the initiation of microscopic cracks tends to generate high-frequency AEs, while the development of macroscopic cracks commonly generates relatively low-frequency AEs, and the medium-frequency AEs are related to friction sliding.<sup>2,62</sup> In other words, the distribution of the AE signal in the frequency domain can reflect the properties of the fractures, especially the size and the fracture mode. The macro-crack initiation and propagation before the peak stress contain multiple cracking mechanisms: microcrack coalescence, macrocrack initiation, new microcracks (transgranular or intergranular), and frictional sliding among grains. The complicated characteristics of the AE frequency are highly correlated to the diversity of the cracking mechanism. The present results also coincide with this conclusion. The reduction in the APF at the beginning of the HGP stage is thought to correspond to the micro-crack coalescence, and the sharp decrease in the APF before the peak stress is related to the macrocrack initiation and coalescence. Such mixed cracking mechanisms increase the AE bandwidth.

## 2. Flaw morphology and AE characteristics

The effect of the flaw morphology on the AE characteristics in the failure process is discussed from the event and energy rates in this section. The flaw morphology includes the number of flaws, the flaw inclination angle  $\alpha$ , and the bridging angle  $\beta$ . **Figures 10** and **11** illustrate the variation in the event rate and energy rate of eight typical double-flawed samples. Multiple peaks of the AE rate are observed before the sample failure, while the event and energy rates differ significantly among different samples. All the samples have a clear three-stage characteristic of the AE event based on the

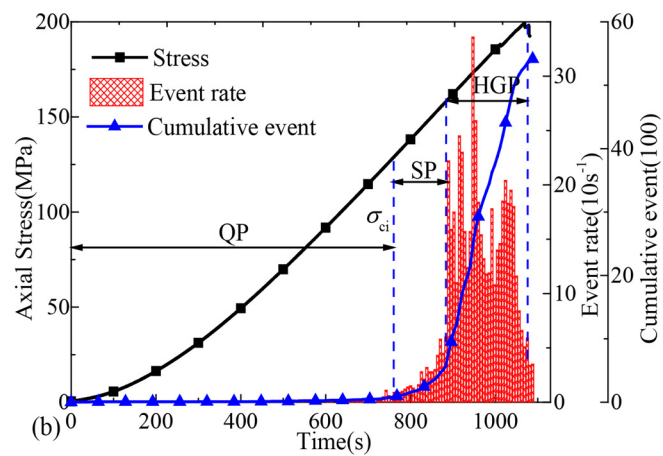
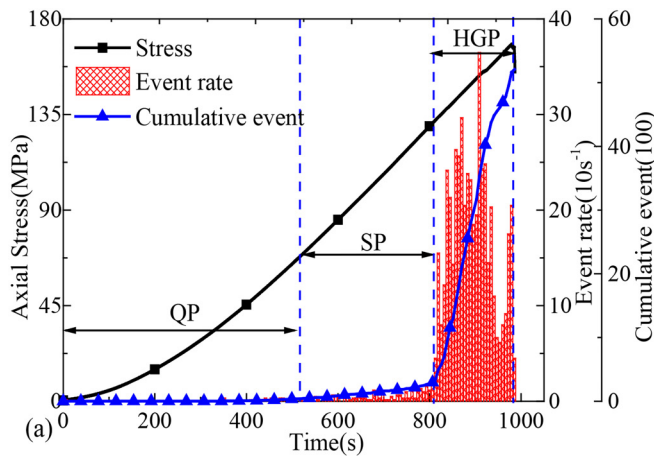


FIG. 12. The event rate and cumulative events of samples with a single flaw: (a)  $\alpha = 45^\circ$  and (b)  $\alpha = 60^\circ$  in the cracking process.

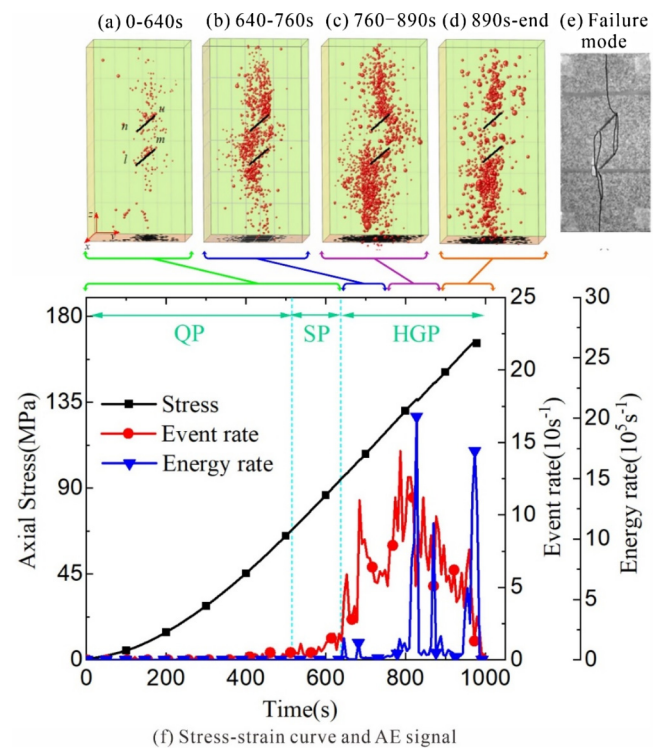
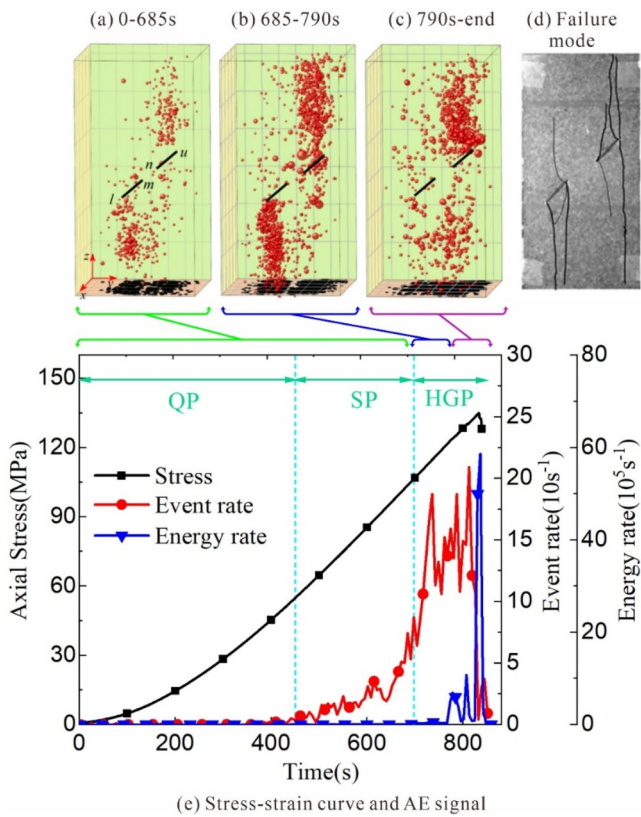


FIG. 13. Spatiotemporal evolution of AE hypocenters at different stages: (a) 0–685 s (before HGP stage); (b) 685–790 s (126 MPa); (c) 790 s-loading end; (d) crack failure patterns; and (e) the corresponding stress–strain curve and AE signal for sample D45–30.

FIG. 14. Spatiotemporal evolution of AE hypocenters at different stages: (a) 0–640 s (before HGP stage); (b) 640–760 s (121.5 MPa); (c) 760–890 s; (d) 890 s-loading end; (e) crack failure patterns; and (f) the corresponding stress–strain curve and AE signal for sample D45–120.

event and energy rates. With an increase in  $\beta$ , the number of AE peaks increases gradually. Meanwhile, the duration and cumulative events of the SP stage (the stable micro-crack growth) decrease regardless of the flaw inclination angle  $\alpha$ . The duration of the SP stage of the samples with  $\alpha = 45^\circ$  is universally longer than those with  $\alpha = 60^\circ$ . However, the QP durations for different samples seem very close, as shown in Figs. 10 and 11, and the QP durations of samples with  $\beta = 90^\circ$  have the shortest duration for both  $\alpha = 45^\circ$  or  $60^\circ$ .

Conspicuous peaks of the AE rate are observed, accompanying the sudden stress drops of the strain-stress curve before the rock failure. The stress drops indicate that stress redistribution and crack initiation always occur with the reduction in the deformation modulus at the following stage. Several characteristic stresses are selected to depict the stress variation in the loading process, as summarized in Table III. They correlate with the beginning of the HGP stage, the maximum event rate, and the maximum energy rate in Figs. 10 and 11.

Stress ratio (SR), defined as the ratio of characteristic stress to peak strength, is used to understand the loading percentage better. Generally, the characteristic stress and SR of the beginning of HGP decrease with  $\beta$  except for the sample ( $\beta = 120^\circ$ ), as listed in Table III. The characteristic stress corresponding to the first stress

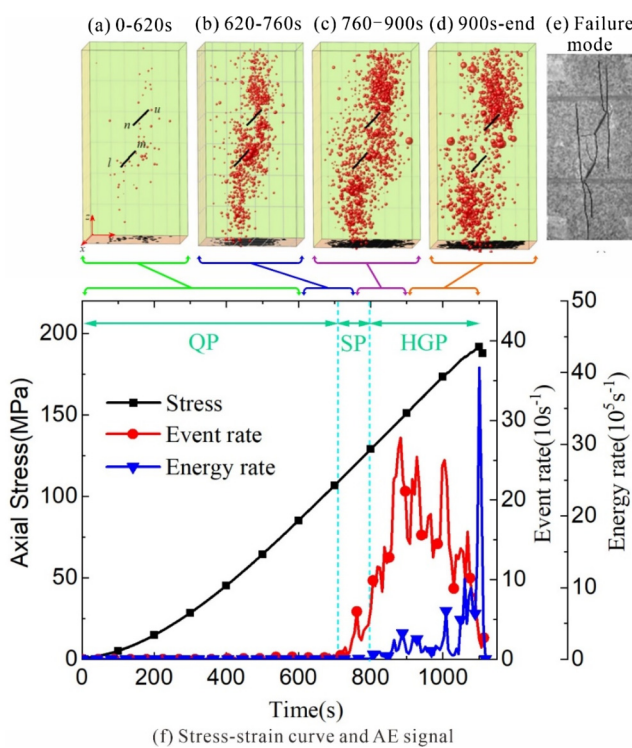


FIG. 15. Spatiotemporal evolution of AE hypocenters at different stages: (a) 0–620 s (before HGP stage); (b) 620–760 s; (c) 760–900 s; (d) 900 s-loading end; (e) crack failure patterns; and (f) the corresponding stress–strain curve and AE signal for sample D60–90.

drop and the maximum event rate have similar variation trends. The beginning of the HGP stage commonly appears earlier than the first stress drop, indicating that the first stress drop occurs only when the number of micro- and macro-cracks reaches a certain threshold. The maximum energy rate occurs much later than the maximum event rate. The SR at the maximum event rate ranges from 0.65 to 0.97, while the maximum energy rate is near the peak strength. The flaw inclination angle also obviously affects these characteristic stresses. The characteristic stresses of  $\alpha = 60^\circ$  samples have a higher value than  $\alpha = 45^\circ$  samples for a certain  $\beta$ . The cumulative number of detected hypocenters and cumulative energy has this trend, too. However, the characteristic stress and SR of the sample with  $\beta = 120^\circ$  turn to increase reversely due to the flaw overlapping.

The variations in the AE event rate and energy rate of single-flawed samples with  $\alpha = 45^\circ$  and  $60^\circ$  (Fig. 12) are compared with the results of double-flawed samples. The three-stage feature of the single-flawed samples is more conspicuous than that of the double-flawed samples. The cumulative AE events, AE energy, and characteristic stresses of single-flawed samples all show higher values. Contrarily, the peak value of the AE rate for the single-flawed

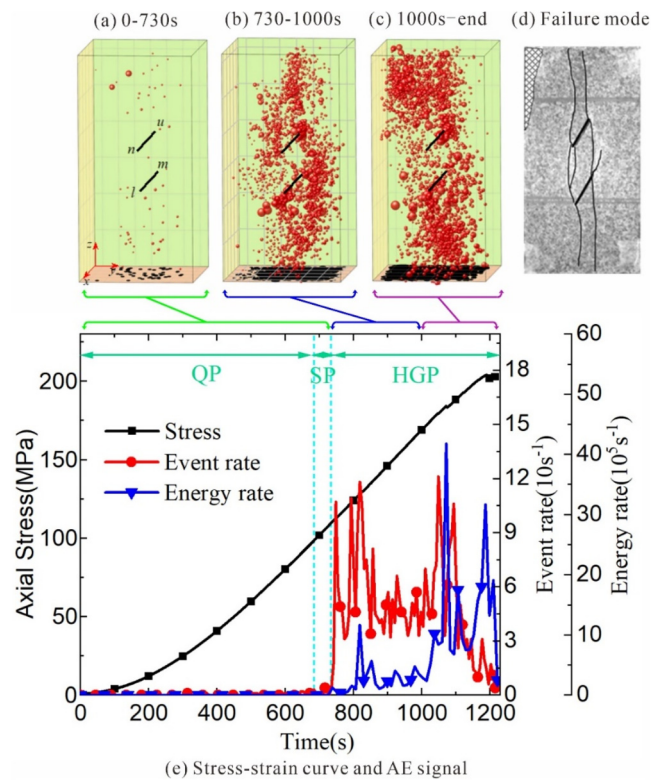


FIG. 16. Spatiotemporal evolution of AE hypocenters at different stages (a) 0–830 s (before HGP stage); (b) 830–1000 s; (c) 1000 s-loading end; (d) crack failure patterns; and (e) the corresponding stress–strain curve and AE signal for sample D60–120.

samples is lower. The result coincides with common sense that fewer defects result in higher strength.

### 3. Spatiotemporal evolution of AE event

The AE hypocenters are projected into a three-dimensional space to study the internal crack propagation. Figure 13 shows the evolutions of the AE hypocenters of sample D45–30. The tips of the pre-existing flaws are marked by *l*, *m*, *n*, and *u*. The red ball represents the AE hypocenters induced by the cracking event, and the hypocenter size is proportional to the signal amplitude or the cracking violence. The development of the AE hypocenters correlates well with the crack development observed from the sample surface. (1) Microcrack initiation is first observed near the flaw-tips. (2) Most hypocenters cluster around the outer flaw-tips before the

HGP stage [Fig. 13(a)]. (3) The AE event rate increases sharply with the hypocenters mainly distributing along the loading direction through the outer flaw-tips at the beginning of the HGP stage [Fig. 13(b)]. (4) These AE hypocenters then coalesce into macrocracks at the outer flaw-tip and propagate through the sample end. (5) After 790 s, AE hypocenters mostly gather near the flaw end *u*, indicating more active cracking events. In the entire cracking process, only a few hypocenters emerge at the bridging zone, coinciding with the observation of no crack coalescence between two pre-existing flaws.

For the samples evolving coalescences between pre-existing flaws like sample D45–120, the evolution process is roughly similar to previous sample D45–30 (Fig. 14). The differences are (1) hypocenters mostly gather at the bridging zone before the HGP stage for sample D45–120; (2) the hypocenter number is less without

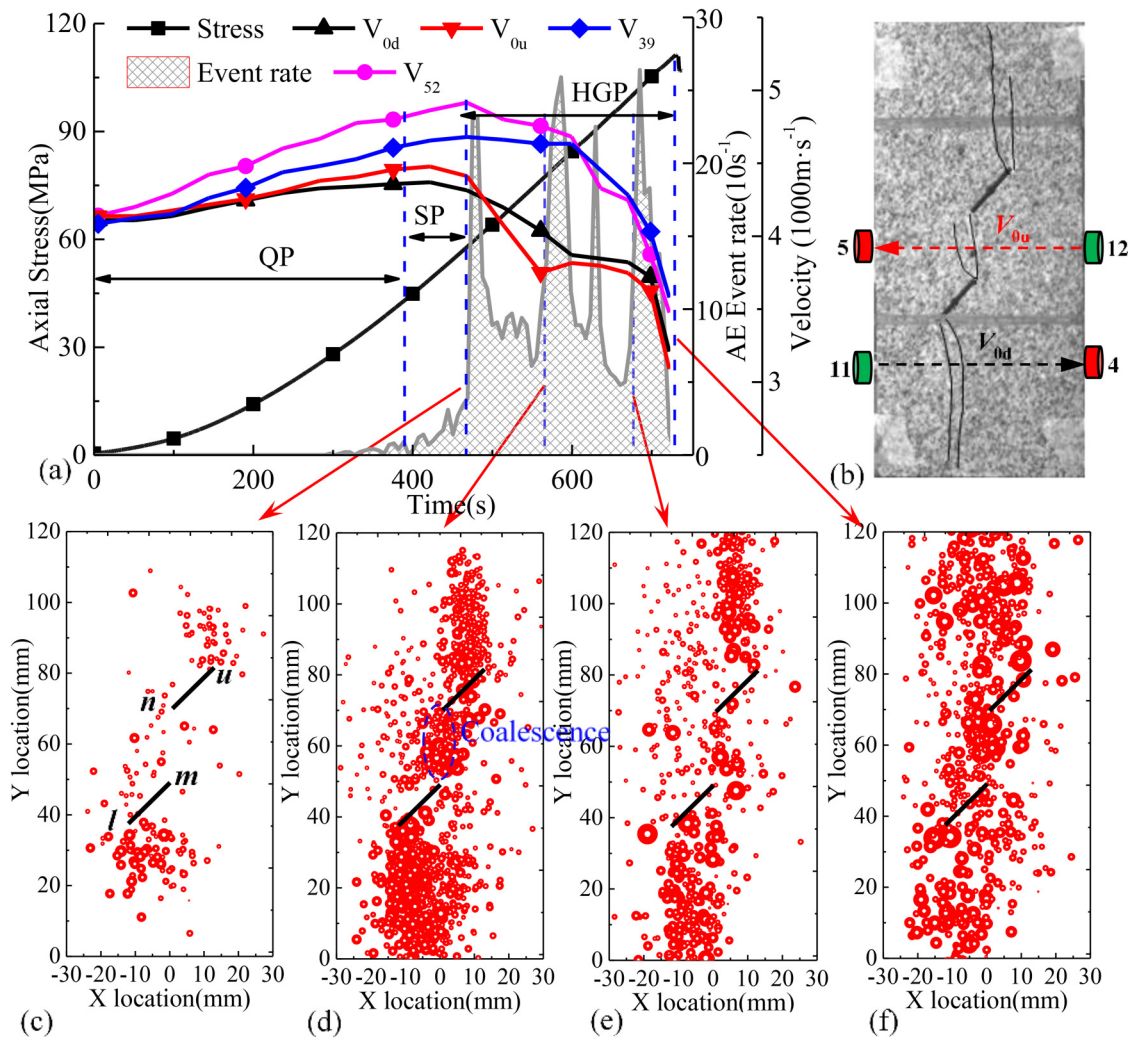


FIG. 17. P-wave velocities and AE events of sample D45–90 in the failure process.

remarkable hypocenter cluster before the HGP stage; and (3) hypocenter clusters developing at the bridging zone evolve to the crack coalescence after 640 s. In 640–890 s, hypocenters distribute near the flaw-tips and propagate in the tensile-wing and anti-wing crack modes. Afterward, hypocenters propagate along the existing paths, coinciding with the failure patterns. The spatiotemporal evolutions of AE hypocenters for samples D60–90 and D60–120 (Figs. 15 and 16) have close behavior with D 45–120 but with a slight difference in the number of AE hypocenters.

Overall, the AE hypocenters can monitor the coalescence initiation process between two flaws well. More AE hypocenters are observed in the samples with a higher inclination angle ( $\alpha = 60^\circ$ ), which indicates more energy for the microcrack initiation. Such a finding coincides with the higher peak stress and other characteristic stresses. Since the hypocenter amplitude is highly correlated to the microcrack size,<sup>2</sup> the amplitude of most hypocenters during the

QP and SP stages is much smaller than those in the HGP stage. Moreover, the hypocenter amplitude tends to increase gradually, and most high-amplitude hypocenters are observed before the peak failure, mainly attributed to the macrocrack coalescence.

#### 4. P-wave velocity and crack evolution

This section utilizes active ultrasonic-wave testing to analyze the variation in the P-wave velocity in the failure process, especially after the initiation of macrocracks and coalescences. Like AE, the variation in the P-wave velocities also correlates well with the cracking process.

Figure 17 shows the P-wave velocities ( $V_{0d}$ ,  $V_{0u}$ ,  $V_{39}$ , and  $V_{52}$ ), the stress-strain curves, and the AE events of sample D45–90. During the initial loading stage, P-wave velocities increase due to the pressure-induced crack closure, while the orientated crack

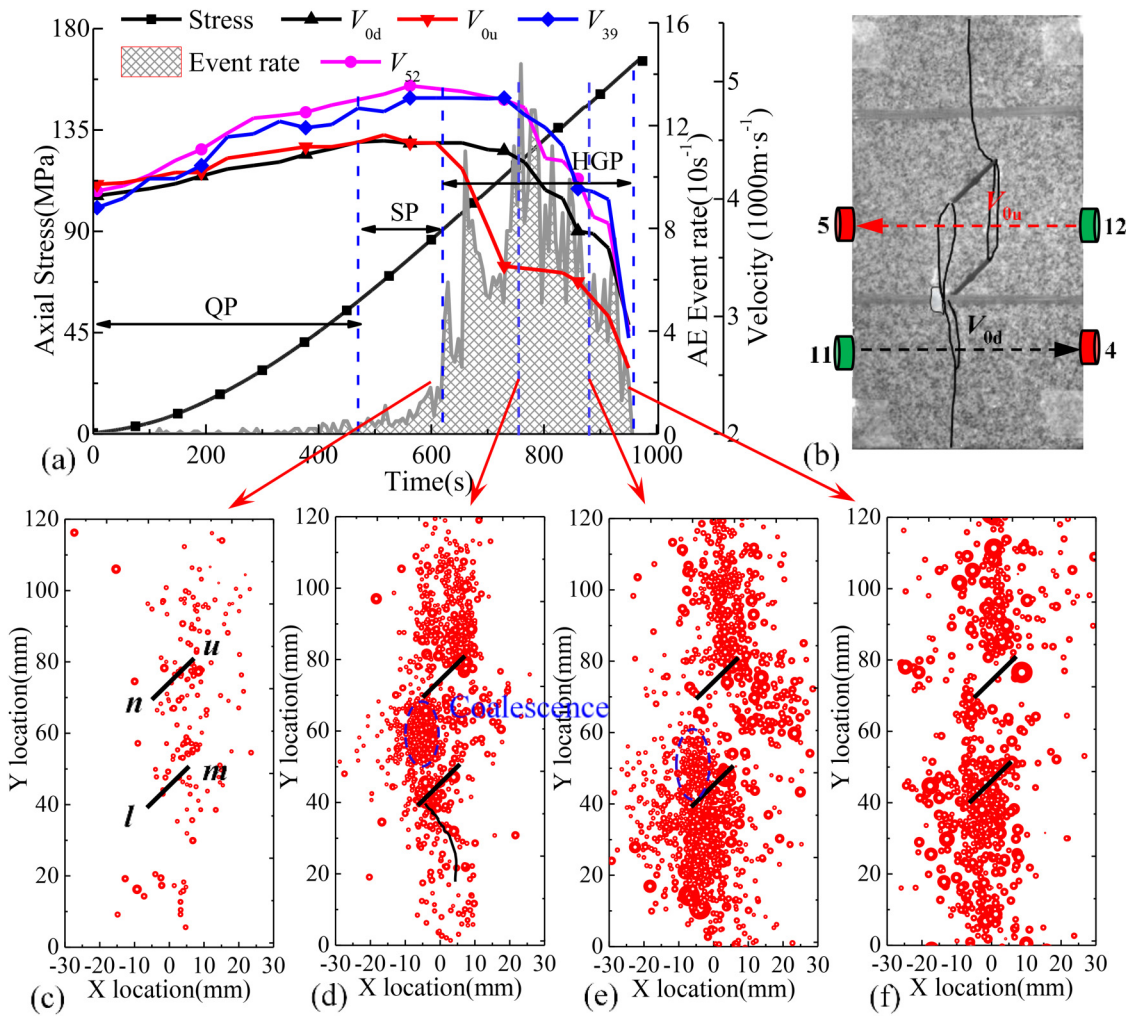


FIG. 18. P-wave velocities and AE events of sample D45–120 in the failure process.

closure results in the differentiation in the velocity increment in different directions. Before the end of the SP stage,  $V_{0u}$  and  $V_{0d}$  reduce gradually at a moderate rate due to the initiation of micro-cracks reflected by the increase in the AE event rate and the gathering of AE hypocenters near the flaw-tips  $l$  and  $u$ . After SP, the P-wave velocities, especially  $V_{0u}$  and  $V_{0d}$ , decrease obviously and intermittently with the macrocrack development. From 485 to 585 s,  $V_{0u}$  and  $V_{0d}$  drop as there is a significant increase in the AE event rate, as shown in Fig. 17(d). Since the AE hypocenters gathering near the inner flaw-tips  $m$  and  $n$  coalesce into clusters before 585 s, the sharp reduction of  $V_{0u}$  coincides with the crack coalescence in the bridging area. Meanwhile, the initiation and propagation of wing cracks, indicated by many AE hypocenters gathering near the outer flaw-tips  $l$  and  $u$ , rapidly reduce the P-wave velocity. In this stage, the decrement of  $V_{0u}$  and  $V_{0d}$  at 585 s reaches 16% and 9.5%, respectively.

Only some scattered hypocenters are observed along the raypath of  $V_{0u}$  (bridging zone) in Fig. 17(e), with little wave speed variation when continuing the axial load. Conversely, hypocenters

are mainly located at the outer flaw-tips propagating to the sample end, which significantly affects the attenuation of  $V_{39}$  and  $V_{52}$ . The decrease of  $V_{39}$  and  $V_{52}$  at 690 s reached 8.5% and 11.5%, respectively. Then, to the final failure, the fast development of macro-cracks reduces the P-wave velocities dramatically. Prior to the complete failure, the decrements of  $V_{0u}$ ,  $V_{0d}$ ,  $V_{39}$ , and  $V_{52}$  reach up to 31%, 27%, 23.5%, and 27.5%. The P-wave velocities of the sample D45–120 have a similar trend with sample D45–90 (Fig. 18). Before the sample failure, the decrements of  $V_{0u}$ ,  $V_{0d}$ ,  $V_{39}$ , and  $V_{52}$  reach 43.7%, 35%, 42%, and 42.5%, which are much higher than those of sample D45–120.

The influences of the bridging angle  $\beta$  on the P-wave velocities of four double-flawed specimens with an inclination angle of 45° or 60° are summarized in Figs. 19 and 20. The variation in P-wave velocities includes several typical stages: (1) gradual increase before micro-crack initiation, (2) differentiation at the SP stage, (3) sharp reduction at the macro-crack initiation, (4) the platform stage (especially  $V_0$ ), and (5) the significant reduction before peak failure. It seems that a certain number of microcracks will not

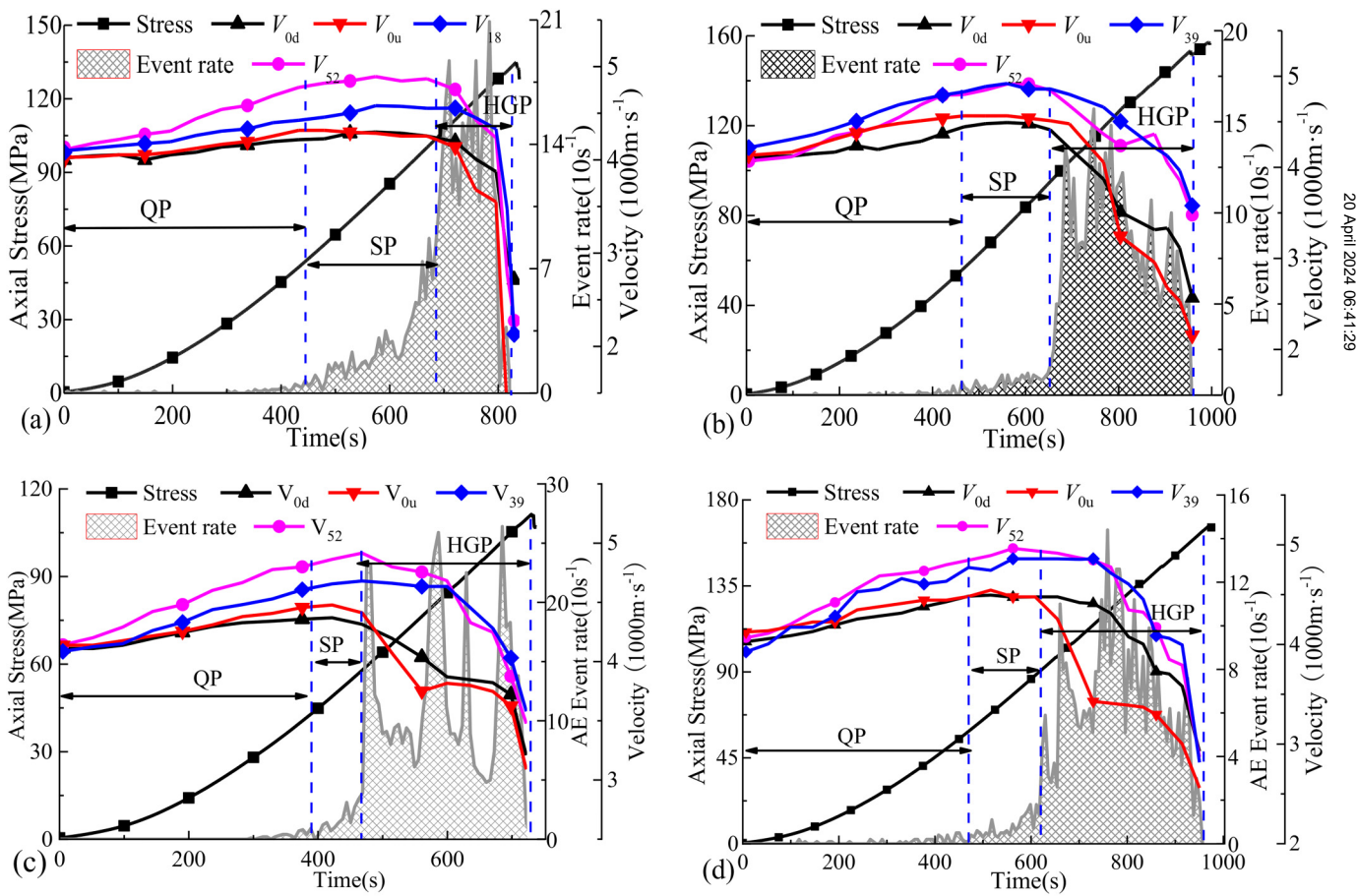
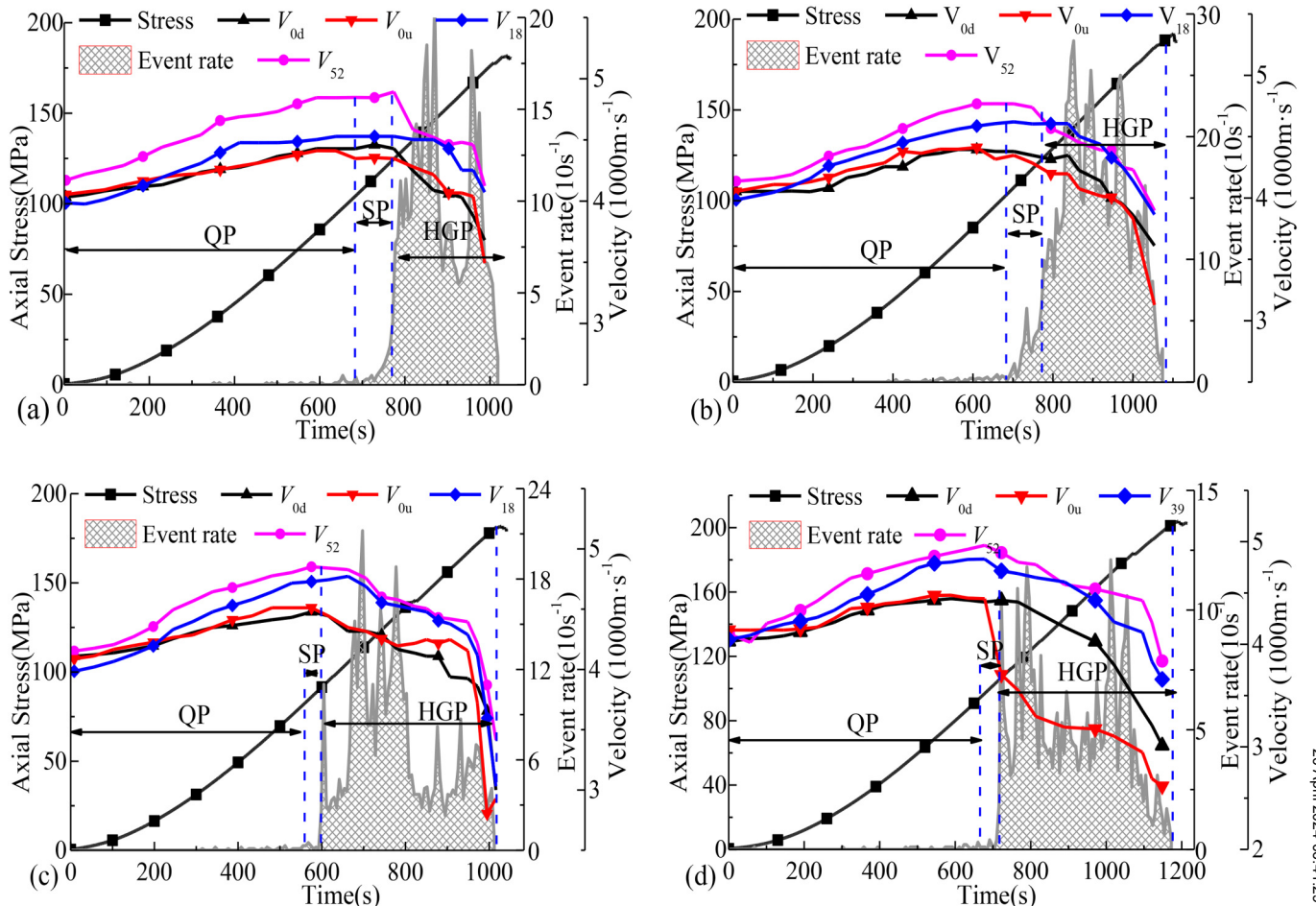


FIG. 19. AE events and P-wave velocities of granite samples containing two parallel flaws with the flaw inclination angle  $\alpha = 45^\circ$  and the bridging angles (a)  $\beta = 30^\circ$ , (b)  $\beta = 60^\circ$ , (c)  $\beta = 90^\circ$ , and (d)  $\beta = 120^\circ$ .



**FIG. 20.** AE events and P-wave velocities of granite samples containing two parallel flaws with the flaw inclination angle  $\alpha = 60^\circ$  and the bridging angles (a)  $\beta = 30^\circ$ , (b)  $\beta = 60^\circ$ , (c)  $\beta = 90^\circ$ , and (d)  $\beta = 120^\circ$ .

reduce the wave velocities at the early stage of loading, and only a significant increase of cracks at the beginning of the HGP stage can produce the dramatic velocity reduction, which can also be found in Table III. In summary, active P-wave testing can detect the cracking zone of rocks and quantify the damage anisotropy.

#### IV. DISCUSSION AND CONCLUSIONS

The present study uses two acoustic methods, the passive AE method and the active P-wave method, to investigate the relationship between the cracking behavior of granite and the acoustic feature in three-dimensional space under uniaxial compression. Mechanical properties, including  $\sigma_c$ ,  $\varepsilon_c$ ,  $E$ ,  $\sigma_{ci}$ , and  $E_{50}$ , are analyzed according to the stepwise stress-strain curves of flawed granites.

- The AE events of all flawed samples can be divided into three stages: QP, SP, and HGP, based on the analysis of the AE event

rate and energy rate. It should be noted that the recorded AE events are only a part of the actual emission events. It was reported that the detected AE events accounted for much less than the total micro-crack damage.<sup>43</sup> A large number of AE signals released quickly, especially before peak failure, may cause the superposition of discrete waveforms. Since the AE hit and ring count are highly dependent on the recording threshold, the hit count representing the waveform number cannot estimate the crack amplitude. In addition, the coalescence of pre-existing cracks leads to the reflection of AE waves, resulting in reduced detected event numbers. However, the AE energy can characterize the crack number and its amplitude well. It is suggested that the damage accumulation by AE energy at the stage of the unstable crack growth, especially prior to peak failure, be evaluated as the cumulative energy is less sensitive to the micro-crack initiation. Thus, the integration analysis using AE event and energy together can give us a thorough understanding of the damage process.

- Compared with intact and single-flawed granite, more stress drops are observed for double-flawed samples, while the three-stage feature of the AE event is more remarkable for single-flawed samples with higher cumulative events and energy.
- The AE hypocenters can effectively monitor the initiation and propagation of the coalescences between two flaws and the development of internal cracks in a three-dimensional space. P-wave velocity is generally well correlated to the AE event and provides more information about the internal damage. Velocity attenuation is more sensitive to the macrocracks but less sensitive to the microcracks in the early stage. Such a feature can be used to detect the macrocracks before and after sample failure. The joint application of the AE method and the active ultrasonic-wave method can more effectively localize and predict the different scales of cracks or damage levels of rocks.
- Compared to the AE method, active ultrasonic testing is convenient and insensitive to environmental disturbances, especially in the *in situ* field test. However, the wave attenuation is highly sensitive to the sensor resonant frequency and the crack size. With the increase in the wave frequency or the decrease in the wavelength, the sensitivity of wave attenuation to rock intrinsic defects increases,<sup>41</sup> which might constrain the application of the ultrasonic method in the *in situ* field. It needs further investigation. On the other hand, as the number of ultrasonic sensors attached to rock surfaces in laboratory testing is limited, only the wave velocities in some specific directions can be measured. Since the P-wave test is not very sensitive to early microcracks, which is the advantage of the AE method, combining AE monitoring and active ultrasonic testing can provide a comprehensive understanding of the fracture process.

In summary, the results indicate that the combination of two acoustic methods can overcome the shortages of each method and enhance the monitoring performance. It provides a solution if there is no available method that is sensitive and economical in monitoring the whole cracking process.

## LIST OF SYMBOLS AND NOMENCLATURE

AE	Acoustic emission
APF	The average peak frequency
$\alpha, \beta$	The flaw angle and bridging angle
D $\alpha$ - $\beta$	Sample containing two parallel flaws with flaw angle $\alpha$ and bridging angle $\beta$
$E_{50}, E$	Deformation modulus and elastic modulus
$\epsilon_c$	Axial strain value at the peak strength
QP, SP, HGP	AE quiet period, stable period, and high growth period
S $\alpha$	Sample containing single flaw with flaw angle $\alpha$
$\sigma_c$	Uniaxial compression strength
$\sigma_{ci}, R_{ci}$	Crack initiation stress and its ratio to peak strength
SR	The ratio of characteristic stress value to peak strength
$V_{0d}$	Lateral velocity in the lower cross section of the flaw
$V_k$	P-wave velocity in $k = 18^\circ, 39^\circ, 52^\circ$ direction
$V_{0u}$	Lateral velocity across the bridging area
$2a, 2b$	The flaw length and ligament length

## ACKNOWLEDGMENTS

This work was financially supported by the National Natural Science Foundation of China (NNSFC) (No. 52278504), the Natural Science Foundation of Jiangsu Province (No. BK20220141), and the China Postdoctoral Science Foundation (No. 2020M681610).

## AUTHOR DECLARATIONS

### Conflict of Interest

The authors have no conflicts to disclose.

### Author Contributions

**Guokai Zhang:** Conceptualization (equal); Data curation (equal); Formal analysis (equal); Funding acquisition (equal); Methodology (equal); Software (equal); Writing – original draft (equal). **Haibo Li:** Formal analysis (equal); Project administration (equal); Supervision (equal). **Mingyang Wang:** Formal analysis (equal); Project administration (equal); Supervision (equal). **Zhen Wang:** Formal analysis (equal); Methodology (equal). **Shuxin Deng:** Data curation (equal); Software (equal). **Fei Gao:** Data curation (equal); Software (equal). **Chunjiang Zou:** Conceptualization (equal); Formal analysis (equal); Methodology (equal); Writing – review & editing (equal).

## DATA AVAILABILITY

The datasets generated during and/or analyzed during the current study are available from the corresponding author upon reasonable request.

## REFERENCES

- X. F. Li, H. B. Li, J. C. Li, and Z. W. Li, *Rock Mech. Rock Eng.* **51**, 2373 (2018).
- G. Zhang, H. Li, M. Wang, X. Li, Z. Wang, and S. Deng, *J. Geophys. Eng.* **16**, 599 (2019).
- X. Chang, S. Wang, Z. Li, and F. Chang, *Constr. Build. Mater.* **360**, 129440 (2022).
- R. H. C. Wong and K. T. Chau, *Int. J. Rock Mech. Mining Sci.* **35**, 147 (1998).
- B. Shen, O. Stephansson, H. H. Einstein, and B. Ghahreman, *J. Geophys. Res.: Solid Earth* **100**, 5975 (1995).
- A. Bobet and H. H. Einstein, *Int. J. Rock Mech. Mining Sci.* **35**, 863 (1998).
- Y.-P. Li, L.-Z. Chen, and Y.-H. Wang, *Int. J. Solids Struct.* **42**, 2505 (2005).
- R. H. C. Wong, K. T. Chau, C. A. Tang, and P. Lin, *Int. J. Rock Mech. Mining Sci.* **38**, 909 (2001).
- H. Lee and S. Jeon, *Int. J. Solids Struct.* **48**, 979 (2011).
- C. H. Park and A. Bobet, *Int. J. Rock Mech. Mining Sci.* **46**, 819 (2009).
- M. Sagong and A. Bobet, *Int. J. Rock Mech. Mining Sci.* **39**, 229 (2002).
- L. N. Y. Wong and H. H. Einstein, *Rock Mech. Rock Eng.* **42**, 475 (2009).
- L. Liu, H. Li, X. Li, D. Wu, and G. Zhang, *Rock Mech. Rock Eng.* **54**, 857 (2021).
- C. Zou, V. Maruvanchery, X. Zhao, and L. He, *Geomech. Geophys. Geo-Energy Geo-Resource* **8**, 20 (2022).
- H. Wang, H. Li, L. Tang, X. Ren, Q. Meng, and C. Zhu, *J. Rock Mech. Geotech. Eng.* **14**, 757 (2022).
- Z. Liu, P. Cao, K. Li, F. Wang, T. Dong, and J. Liu, *Bull. Eng. Geol. Environ.* **81**, 61 (2022).
- Y. Zhao, J. Liao, Y. Wang, Q. Liu, H. Lin, and L. Chang, *Arabian J. Geosci.* **13**, 1251 (2020).

- <sup>18</sup>L. N. Y. Wong and H. H. Einstein, *Geotech. Testing J.* **32**, 164 (2009).
- <sup>19</sup>L. Liu, H. Li, and X. Li, *J. Rock Mech. Geotech. Eng.* **14**, 2034 (2022).
- <sup>20</sup>Z. Zhong, D. Huang, Y. Song, and D. Cen, *Int. J. Rock Mech. Mining Sci.* **159**, 105196 (2022).
- <sup>21</sup>S. Huang, J. Wang, Y. Liu, Q. Tian, and C. Cai, *Theor. Appl. Fract. Mech.* **123**, 103669 (2023).
- <sup>22</sup>S.-Q. Yang, *Eng. Fract. Mech.* **78**, 3059 (2011).
- <sup>23</sup>C. Liu, D. D. Pollard, and B. Shi, *J. Geophys. Res.: Solid Earth* **118**, 71 (2013).
- <sup>24</sup>Z. Wu, L. Fan, Q. Liu, and G. Ma, *Eng. Geol.* **225**, 49 (2017).
- <sup>25</sup>L. F. Fan, X. F. Zhou, Z. J. Wu, and L. J. Wang, *Tunnelling Underground Space Technol.* **92**, 103032 (2019).
- <sup>26</sup>Y. Wang, J. Q. Han, and C. H. Li, *Constr. Build. Mater.* **260**, 119769 (2020).
- <sup>27</sup>E. Eberhardt, D. Stead, B. Stimpson, and R. S. Read, *Can. Geotech. J.* **35**, 222 (1998).
- <sup>28</sup>M. S. Diederichs, P. K. Kaiser, and E. Eberhardt, *Int. J. Rock Mech. Mining Sci.* **41**, 785 (2004).
- <sup>29</sup>P. Ganne and A. Vervoort, *Int. J. Fract.* **144**, 77 (2007).
- <sup>30</sup>J. Vilhelm, V. Rudajev, T. Lokajíček, and J. Veveřka, *Rock Mech. Rock Eng.* **41**, 695 (2008).
- <sup>31</sup>S. Miao, P.-Z. Pan, Z. Wu, S. Li, and S. Zhao, *Eng. Fract. Mech.* **204**, 319 (2018).
- <sup>32</sup>S. Zhang, S. Wu, C. Chu, P. Guo, and G. Zhang, *Rock Mech. Rock Eng.* **52**, 2067 (2019).
- <sup>33</sup>J. Browning, P. G. Meredith, C. E. Stuart, D. Healy, S. Harland, and T. M. Mitchell, *J. Geophys. Res.: Solid Earth* **122**, 4395 (2017).
- <sup>34</sup>J. Peng, G. Rong, M. Yao, L. N. Y. Wong, and Z. Tang, *Bull. Eng. Geol. Environ.* **78**, 4479 (2019).
- <sup>35</sup>G. Zhang, M. Wang, X. Li, S. Yue, Z. Wen, and S. Han, *Constr. Build. Mater.* **292**, 123452 (2021).
- <sup>36</sup>S.-Q. Yang, W.-L. Tian, X.-R. Liu, Y.-H. Huang, and J. Yang, *Theor. Appl. Fract. Mech.* **114**, 102975 (2021).
- <sup>37</sup>X. Hu, L. Luo, G. Lei, X. Gong, P. Guo, H. Hu, J. Ma, and S. Wang, *Shock Vib.* **2021**, 7117163.
- <sup>38</sup>J. Li, D. Liu, M. He, Y. Guo, and H. Wang, *Bull. Eng. Geol. Environ.* **82**, 65 (2023).
- <sup>39</sup>P. M. Benson, B. D. Thompson, P. G. Meredith, S. Vinciguerra, and R. P. Young, *Geophys. Res. Lett.* **34**(3), L03303 (2007).
- <sup>40</sup>A. Ougier-Simonin, J. Fortin, Y. Guéguen, A. Schubnel, and F. Bouyer, *Int. J. Eng. Sci.* **49**, 105 (2011).
- <sup>41</sup>S. D. Goodfellow, N. Tisato, M. Ghofranitabari, M. H. B. Nasseri, and R. P. Young, *Rock Mech. Rock Eng.* **48**, 2551 (2015).
- <sup>42</sup>V. Srinivasan, T. Gupta, T. A. Ansari, and T. N. Singh, *Bull. Eng. Geol. Environ.* **79**, 4335 (2020).
- <sup>43</sup>D. Lockner, *Int. J. Rock Mech. Mining Sci. Geomech. Abstr.* **30**, 883 (1993).
- <sup>44</sup>J. Zhao, X. Feng, H. Guo, Y. Hu, G. Chen, and C. Yang, *Bull. Eng. Geol. Environ.* **81**, 520 (2022).
- <sup>45</sup>X. Lei, K. Masuda, O. Nishizawa, L. Jouniaux, L. Liu, W. Ma, T. Satoh, and K. Kusunose, *J. Struct. Geol.* **26**, 247 (2004).
- <sup>46</sup>G. K. Zhang, H. B. Li, M. Y. Wang, J. Li, and S. X. Deng, *Chin. J. Geotech. Eng.* **41**, 1074 (2019).
- <sup>47</sup>B. Q. Li, B. Gonçalves da Silva, and H. Einstein, *Eng. Fract. Mech.* **209**, 200 (2019).
- <sup>48</sup>J. C. Li, L. F. Rong, H. B. Li, and S. N. Hong, *Rock Mech. Rock Eng.* **52**, 403 (2019).
- <sup>49</sup>I. L. Meglis, T. Chow, C. D. Martin, and R. P. Young, *Int. J. Rock Mech. Mining Sci.* **42**, 25 (2005).
- <sup>50</sup>C. Zou, Z. Chen, P. Dong, C. Chen, and Y. Cheng, *J. Bridge Eng.* **21**, 04015040 (2016).
- <sup>51</sup>W. O. Raji and K. O. Aluko, *Bull. Eng. Geol. Environ.* **80**, 6445 (2021).
- <sup>52</sup>J. Martínez-Martínez, N. Fusi, J. J. Galiana-Merino, D. Benavente, and G. B. Crosta, *Eng. Geol.* **200**, 47 (2016).
- <sup>53</sup>T. Lokajíček, R. K. Goel, V. Rudajev, and R. D. Dwivedi, *Int. J. Rock Mech. Mining Sci.* **57**, 142 (2013).
- <sup>54</sup>T. Lokajíček, M. Petružálek, T. Svitek, A. Kuchařová, Š. Šachlová, and R. Přikryl, *Bull. Eng. Geol. Environ.* **80**, 8921 (2021).
- <sup>55</sup>U. Kuila, D. N. Dewhurst, A. F. Siggins, and M. D. Raven, *Tectonophysics* **503**, 34 (2011).
- <sup>56</sup>C. Du, Y. Pan, Q. Liu, X. Huang, and X. Yin, *Bull. Eng. Geol. Environ.* **81**, 499 (2022).
- <sup>57</sup>A. Modiriasari, A. Bobet, and L. J. Pyrak-Nolte, *Rock Mech. Rock Eng.* **50**, 2311 (2017).
- <sup>58</sup>M. Heidari, G. R. Khanlari, M. Torabi-Kaveh, S. Kargarian, and S. Saneie, *Rock Mech. Rock Eng.* **47**, 785 (2014).
- <sup>59</sup>L. N. Y. Wong, C. Zou, and Y. Cheng, *Rock Mech. Rock Eng.* **47**, 1117 (2014).
- <sup>60</sup>N. Y. Wong, Ph.D. thesis (Massachusetts Institute of Technology, 2008).
- <sup>61</sup>P. Rodríguez and T. B. Celestino, *Eng. Fract. Mech.* **210**, 54 (2019).
- <sup>62</sup>M. Ohnaka and K. Mogi, *J. Geophys. Res.: Solid Earth* **87**, 3873 (1982).